Numerical Simulation of Acoustic Streaming in Standing Waves

A.I. Delis[a,*], V. Mandikas[a], H. Guillard[b]

[a] *School of Production Engineering & Management, Technical University of Crete, University Campus, 73100, Chania, Greece*
[b] *INRIA Sophia-Antipolis Mediteranee & University Cote d'Azur, Parc Valrose, 06108, Nice Cedex, France*

Abstract

This study presents a numerical investigation of acoustic streaming motion (of the Rayleigh type) in a compressible gas inside two-dimensional rectangular enclosures. To numerically study the effects of the sound field intensity on the formation process of streaming structures, we propose to discretize the fully compressible form of the two-dimensional Navier-Stokes equations using a high-order (formally greater or equal to fourth-order) accurate numerical scheme in both space and time. The proposed numerical solver utilizes high-order compact schemes along each spatial dimension combined with a filtering procedure when it is necessary. Acoustic standing waves are excited inside the enclosures and the resulting acoustic streaming patterns are investigated for low and high-intensity waves, in both linear and nonlinear regimes following closely the work of Daru et al. (2013). An extended investigation indicates that without the incorporation of an appropriate filter, the application of the high-order compact schemes in case of fast streaming results in spurious oscillations which inhibit their applicability. Following the recent relevant literature, the numerical simulations performed demonstrate the ability of the proposed numerical approach to reproduce efficiently and robustly the transitions from regular acoustic streaming to irregular streaming and the relevant phenomena confirming results that have

*Corresponding author
Email addresses: `adelis@science.tuc.gr` (A.I. Delis), `vmandikas@isc.tuc.gr` (V. Mandikas), `herve.guillard@inria.fr` (H. Guillard)

been previously presented.

Keywords: Acoustic Streaming, Standing Waves, Numerical Simulation, Compact Finite Differences, Higher-order Methods, Regular and Irregular Streaming.

1. Introduction

Acoustic streaming, [1, 2, 3, 4], is a secondary mean steady flow generated by and superimposed on a primary oscillatory flow. When a compressible fluid experiences an oscillatory motion (e.g. from a sound source) the nonlinear interactions can often lead to a pattern of time-dependent vortical flows or steady circulations in the flow field. As such, sound at high-intensity levels in gases and liquids can generate these mean second-order flow patterns. Acoustic streaming can be sorted into several categories based on the different mechanisms by which it is generated [4]. For example, boundary-layer-driven streaming or as it is well-known Rayleigh (or outer) streaming, Eckart or quartz-wind streaming, jet-driven streaming, and traveling-wave or Gedeon streaming. The understanding of acoustic streaming is of both fundamental and practical interest since apart from being an interesting physical phenomenon, it plays an important role (positive or negative) in many applications [5]. For example, in many thermoacoustic devices, acoustic streaming results in convected heat flow that can reduce the device's efficiency.

Rayleigh-type (or outer) streaming is the main focus of this work. In general, Rayleigh acoustic streaming can be generated inside two-dimensional enclosures as a result of the interaction between a plane standing wave and the solid boundaries and the mean second-order flow is produced mainly by shear viscous forces near the fluid-solid boundary. The enclosure's typical geometry is that of length much larger than its transverse dimensions filled with a compressible gas initially at homogeneous pressure and temperature. Rayleigh streaming is associated with a length scale of the same order of magnitude as the wavelength and has a vortex-like structure, characterized by four steady counter-rotating vortices, outside the boundary layer. These vortices develop along the half wavelength (λ) of the standing wave. Vortex motion is also generated inside the viscous boundary layer (with thickness δ_ν) with four additional vortices created simultaneously. The vortex motion inside the boundary layer is called inner or Schlichting streaming [4]. Along the central axis of the enclosure, the streaming motion is oriented from acoustic velocity node to antinodes while in the boundary layers from acoustic velocity antinodes to nodes along the inner walls [3].

The acoustic streaming flow patterns can be categorized into regular (or classical) and irregular ones. The regular streaming appears as two vortices per quarter-wavelength of the standing wave which are symmetric about the enclosure's center line, as schematically shown in Figure 1. In irregular streaming, the shape and number of the streaming vortices are different from the regular case. Closely related to this characterization is the one form [6] where it was shown that the streaming itself can be linear (case of slow streaming) or nonlinear (case of fast streaming). In the case of slow streaming, where the streaming velocity is considerably smaller compared to the acoustic particle velocity, the effect of inertia on the streaming flow can be neglected by comparison with viscous effects. On the other hand, the effect of inertia causes distortions to the streaming patterns and thus cannot be neglected. In [6] a dimensionless parameter characterizing the streaming flow for both linear and nonlinear regimes has been identified; the nonlinear Reynolds number

$$Re_{NL} = \left(\frac{U_0}{c_0}\right)^2 \left(\frac{y_0}{\delta_\nu}\right)^2 = \left(M\frac{y_0}{\delta_\nu}\right)^2, \tag{1}$$

where U_0 is the velocity amplitude of the standing wave, c_0 is the speed of sound, y_0 is the half-width of the enclosure and M is the acoustic Mach number. If $Re_{NL} \ll 1$, the effect of inertia on the streaming flow can be neglected by comparison with viscous effects and we speak about the slow streaming; on the contrary, if $Re_{NL} \gg 1$, the effect of inertia cannot be neglected anymore and we speak about the fast streaming. In the slow regime, the streaming structure does not depend on the acoustic field amplitude, in the fast regime

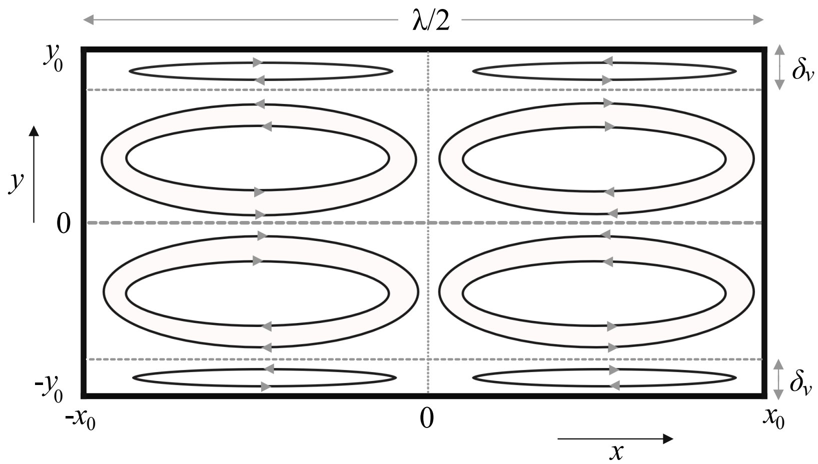

Figure 1: Regular acoustic streaming patterns inside an enclosure

the effect of inertia, according to the theory in [6], causes a specific streaming-profile distortion which increases with the increasing value of Re_{NL}. Large amplitude acoustic oscillations, including shock-type waves, induce streaming of large Re_{NL} in closed resonators and the flow becomes turbulent [2]. In many practical applications of high-intensity resonant oscillations in closed enclosures streaming may be inevitable. Hence, the understanding of nonlinear streaming is of both fundamental and practical interest.

In terms of analytical or semi-analytical modeling of the phenomenon, most such streaming models have been developed for the case of slow streaming, i.e. for $Re_{NL} \ll 1$. Among others, in [7] a fully analytical solution for acoustic streaming generated by a standing wave in a rectangular channel of arbitrary width filled with a viscous fluid was presented employing the methods of perturbation analysis. In [7] it was shown that for streaming inside a resonator, the ratio of the boundary layers thickness (δ_ν) to the resonator's half width (y_0) is an important parameter that describes the behavior of the inner and outer streaming. Further, in [8] the authors generalized their solution to take into account the variations of heat conduction and viscosity with temperature showing that thermal effects have a limited influence on the streaming flow for low amplitude acoustic waves. These analytical solutions are valuable for accessing the accuracy of numerical solutions in the slow streaming regime.

In [9] an experimental study was performed involving streaming for Re_{NL} up to 20 and it was found that the streaming fields are distorted for high nonlinear Reynolds numbers in correlation with the increasing temperature gradient along a streaming cell. Further, in [10] streaming in square enclosures was analyzed based on PIV measurements and it was found that for Re_{NL} values up to 25, streaming cells are regular whereas when Re_{NL} exceeds 25, streaming deforms to irregular and complex shape patterns. These findings where verified experimentally and numerically also in [4, 11, 12, 13, 14]. All the above studies have verified that the longitudinal streaming velocity component along the axis becomes distorted as the acoustic level increase when compared to its sinusoidal form at low acoustic levels. For high acoustic amplitudes, the generation of counter-rotating additional vortices in the center of the enclosure has also been observed, while the near-wall region inner streaming vortices are modified less. Further, in [15], it was shown that inertial effects cannot be considered as the leading phenomenon to explain these distortions and that nonlinear interaction between the streaming flow and acoustics has to be considered. More recently, in [16, 17, 18, 19] the interaction between the mean temperature and the streaming flow at high acoustic levels was analyzed by following a combined formal and phenomenological approach.

Numerical computations for acoustic Rayleigh-type streaming have emerged in the literature in the past few decades and two approaches have been mainly followed. The first one is based on solving the full 2D Navier-Stokes (NS) equations for low and high-intensity acoustic waves and extracting the mean flow from the instantaneous one, we refer for example in [20, 21, 22, 13, 11, 14, 15]. The second one is based on solving streaming equations for the mean flow but in the linear case, for example in [23, 24]. The necessity of utilizing the full 2D NS equations mainly stems from the need to accurately simulate the flow field inside and outside the boundary layer, especially for high amplitude plane standing waves. Hence, the full 2D NS equations can provide a sufficient description of the essential physical mechanisms in all cases.

The numerical computation of acoustic streaming by solving the full 2D Navier-Stokes equations is considered very challenging. Two key factors mainly exist which may degrade the numerical solutions; one arises from the thin boundary layers adjacent to the solid surface and the other from the extremely low levels of the streaming velocities compared with the primary flow. The negative effects of these factors may be alleviated if very fine grids are implemented near the boundary layers and simultaneously use high-precision numerical schemes. Further to the above challenges, the appearance of shock-type wave profiles in the flow for high acoustic levels, [25, 21, 13], may affect the numerical solution due to numerical oscillations if they are not of relative weak intensity. In [21] simulations of acoustic streaming in the linear and nonlinear regime were performed, taking into account heat transfer, in two-dimensional rectangular enclosures by solving the full compressible Navier-Stokes equations with a fourth-order accurate Flux-Corrected Transport (FCT) scheme. The numerical tests in [21] were conducted for Re_{NL} numbers up to 16 and although the results were in agreement with theoretical results in the linear regime and show irregular streaming motion in the nonlinear regime. However, this irregular motion was exhibited at smaller Re_{NL} values in contradiction to the experimental results from [26, 9, 10]. For solving the 2D Navier-Stokes equations in [13], and later in [11, 14, 15], a finite volume upwind scheme, with third-order accuracy in space and time for the convective terms, and a centered second-order scheme for the diffusion terms was implemented. The numerical simulations performed in [13] demonstrated the transition from regular acoustic streaming flow towards irregular streaming, in agreement with experimental data, demonstrated also that there is an intricate coupling between the mean temperature field and the streaming flow. We note here that, the relevant literature concerning numerical investigations of acoustic is rather limited up to this date, especially for nonlinear streaming regimes.

Alternatively, to numerical methods used thus far for solving the full 2D Navier-Stokes equations for acoustic streaming, compact higher-order finite difference schemes can provide an effective way of combining the robustness of local methods (in the sense that computes the derivatives using neighboring nodes) and the accuracy of spectral methods (global methods). The computation of derivatives in compact finite differences is implicit in the sense that the derivatives are computed in a coupled fashion along an entire line [27]. Such an approach yields a global scheme without sacrificing the advantage of low computational cost and robustness of a scheme on a local stencil, since solving the resulting tri-diagonal linear system can be carried out very efficiently, [28], for serial programming and vector parallelism [29, 30]. In particular, the proposed GPU tri-diagonal solver in [29] can achieve up to a $28\times$ speedup over a sequential LAPACK solver for a 512×512 computation grid. Another advantage of the compact scheme discretizations is that the resulting linear systems to be solved are of the tri-diagonal form. In [30], taking into account the structure of these matrices, the matrix-free storage method allows the entire computation to be executed on the accelerator device, minimizing memory communication costs. Further, compared to the standard finite difference approximations, compact schemes have improved resolution in wave-space [27, 31, 32], i.e compact schemes provide a better representation of the shorter length scales when applied to problems with a range of spatial scales such as flows for high acoustics levels, e.g acoustic resonances occurring within a compressor. Extensive study and discussion of the resolution characteristics of the higher-order compact schemes on uniform grids have been carried out in [27]. In the last decades, many applications of high-order compact differential schemes are presented including numerical simulations of incompressible [33, 34, 35] and compressible flows [36]. However, one of the principal problems encountered in the solution of Navier-Stokes equations with centered schemes, like compact schemes, is the appearance of numerical instabilities, typically arising near boundaries, in regions of mesh non-uniformities, or in the presence of shock waves or solutions involving steep gradients. For such cases, an adaptive filtering technique [37] can provide a robust improvement.

We advocate that higher-order compact finite difference (HCFD) numerical schemes may have several advantages when used for simulating Rayleigh acoustic streaming. The main advantage of the HCFD scheme considered is its ability to accurately capture high-frequency content in the solution, such as sharp gradients and oscillations, while maintaining numerical stability. This makes them particularly useful at the considered problem. In summary, the advantages of HCFD schemes for Rayleigh acoustic streaming computations are:

- High accuracy: Higher-order HCFD schemes are capable of achieving high accuracy, which is important for simulating the complex flow patterns that occur in acoustic streaming. These schemes can accurately resolve small-scale vortices and other flow features, which are essential for understanding the mechanisms underlying the phenomenon.

- Ability to capture sharp gradients: nonlinear acoustic streaming involves sharp gradients in the acoustic pressure and velocity fields. HCFD schemes are well-suited for resolving these gradients, as they use higher-order derivatives in their approximations. This makes them capable of accurately capturing the flow patterns and vortices that occur in Rayleigh acoustic streaming.

- Efficient handling of complex geometries: HCFD schemes are well-suited for handling complex geometries, such as the irregular shapes of cavities and channels that may be used in acoustic streaming experiments. HCFD schemes can be adapted to non-uniform grids and irregular boundaries, making them suitable for simulations of real-world applications.

- Numerical stability: HCFD schemes are designed to maintain numerical stability while achieving high accuracy. This is essential for simulating turbulent flows and other complex flow phenomena that may occur in Rayleigh acoustic streaming. Inclusion of the filter restores the advantages of high-order approach even in the presence of sharp gradients and discontinuities.

- Ease of implementation: HCFD schemes are relatively easy to implement and require minimal programming effort. Further, using OpenMP for parallelization can provide significant advantages in terms of increased speed, scalability, portability, reduced memory requirements, and improved code maintainability.

- Compared to the finite volume (FV) schemes that have been applied thus far for the acoustic streaming problem, FV schemes may require more computational resources than HCFD schemes to achieve the same level of accuracy. Moreover, although in [13] a third-order scheme has been used for the convective terms of the equations a second order centerded scheme has been implemented for the diffusion terms which reduces the formal order of accuracy. On the other hand HCFD schemes use higher-order derivatives in their approximations, which reduces the truncation error and improves global accuracy.

In brief, we consider that HCFD numerical schemes are well-suited for simulating Rayleigh acoustic streaming due to their high accuracy, ability to capture sharp gradients, efficient handling of complex geometries, numerical stability, and computational efficiency.

To the best of our knowledge, there is no literature concerning investigations about either the application of the compact finite difference method or the effects of its filtering components on acoustic streaming flow computations due to the possible appearance of shock-type waves. Thus, this study proposes, for the first time, a compact finite difference method as the discretization scheme of choice for the 2D compressible Navier-Stokes equations to compute the acoustic streaming in both linear and non-linear regimes. We aim to numerically study the distortion of the Rayleigh streaming structures as have been reported in the literature, following closely the work and set-up presented in [13], for comparison purposes. To this end, plane standing waves of different intensities are exited inside rectangular enclosures and the effects of the sound field intensity on the formation process of streaming structures are investigated numerically for various Re_{NL} numbers ranging from slow to fast acoustic streaming. Further, we aim to give a detailed presentation of the proposed numerical scheme in terms of the different options for its implementation concerning its order of discretization near the boundaries as well as the different options on the numerical filtering and produce some concrete recommendations on their applicability to the problem at hand.

2. Model problem and governing equations

We consider a rectangular undeformable enclosure of length L and half-width y_0 that has isothermal and no-slip walls, filled with the working gas. To investigate the formation of streaming flow structures, we need to initiate an acoustic standing wave in the enclosure. To this end, the enclosure is vibrated in the longitudinal direction, x, by imposing on it a harmonic velocity law in time t; that is $\mathbf{V}(t) = [V(t), 0]^{\mathrm{T}}$, where $V(t) = \omega x_{\max} \cos(\omega t)$, with $\omega = 2\pi f$ being the angular vibration frequency, f the vibration frequency of the enclosure and $x_{\max}$ its maximum displacement.

The flow field is modeled by the compressible two-dimensional Navier-Stokes equations expressed in the moving frame attached to the enclosure so that a vibration forcing term is added [13]. The model equations in conservative form in a Cartesian coordinate system then read as

$$\frac{\partial \mathbf{U}}{\partial t} + \frac{\partial(\mathbf{F} - \mathbf{F}_\nu)}{\partial x} + \frac{\partial(\mathbf{G} - \mathbf{G}_\nu)}{\partial y} = \mathbf{S}, \tag{2}$$

where

$$\mathbf{U} = \begin{pmatrix} \rho \\ \rho u \\ \rho v \\ \rho E \end{pmatrix}, \ \mathbf{F} = \begin{pmatrix} \rho u \\ \rho u^2 + p \\ \rho u v \\ u(\rho E + p) \end{pmatrix}, \ \mathbf{G} = \begin{pmatrix} \rho v \\ \rho u v \\ \rho v^2 + p \\ v(\rho E + p) \end{pmatrix}, \tag{3}$$

$$\mathbf{F}_\nu = \begin{pmatrix} 0 \\ \tau_{xx} \\ \tau_{xy} \\ \tau_{xx}u + \tau_{yx}v + k\dfrac{\partial T}{\partial x} \end{pmatrix}, \mathbf{G}_\nu = \begin{pmatrix} 0 \\ \tau_{xy} \\ \tau_{yy} \\ \tau_{xy}u + \tau_{yy}v + k\dfrac{\partial T}{\partial y} \end{pmatrix}, \mathbf{S} = \begin{pmatrix} 0 \\ -\rho\dfrac{dV}{dt} \\ 0 \\ -\rho u\dfrac{dV}{dt} \end{pmatrix}, \tag{4}$$

where ρ is the density, u and v the flow velocity components in $x-$ and $y-$direction, respectively, p denotes the pressure, μ the dynamic viscosity, E the total energy per unit mass, T is the temperature and k is the thermal conductivity. The viscous stress tensor components are

$$\tau_{xx} = 2\mu\frac{\partial u}{\partial x} - \frac{2}{3}\mu\left(\frac{\partial u}{\partial x} + \frac{\partial v}{\partial y}\right), \tag{5}$$

$$\tau_{yy} = 2\mu\frac{\partial v}{\partial y} - \frac{2}{3}\mu\left(\frac{\partial u}{\partial x} + \frac{\partial v}{\partial y}\right), \tag{6}$$

$$\tau_{xy} = \tau_{yx} = \mu\left(\frac{\partial v}{\partial x} + \frac{\partial u}{\partial y}\right). \tag{7}$$

The pressure p and the temperature T are given by the equations of state for a perfect gas, which can be expressed as

$$p = (\gamma - 1)\left(\rho E - \frac{1}{2}(u^2 + v^2)\right), \tag{8}$$

$$T = \frac{p}{R\rho}, \tag{9}$$

where $\gamma = \dfrac{c_p}{c_v}$ is the ratio of specific heats at constant volume and pressure, respectively, and R is the perfect gas constant corresponding to the working gas. The speed of sound c is related to the pressure and density by $c^2 = \gamma\dfrac{p}{\rho}$. In this study, the thermo-physical properties μ and k are assumed to be constant. Finally, the Prandtl, Pr, number is the constant that relates thermal conductivity to viscosity defined as $Pr = \dfrac{\mu c_p}{k}$ with $c_p = \dfrac{\gamma R}{\gamma - 1}$.

We seek to investigate numerically the acoustic streaming generated by the interaction of the enclosure's walls and the imposed plane standing wave. To this end, resonant conditions are imposed, for which the enclosure's length $L = \lambda/2$, $\lambda = c_0/f$ being the wavelength with $c_0 = \sqrt{\gamma p_0/\rho_0}$ being the speed of sound at the initial state. It is well-known, [7, 8], that boundary layers develop along the walls, with acoustic boundary layer thickness $\delta_\nu = \sqrt{2\nu/\omega}$ where ν is the kinematic viscosity $\nu = \mu/\rho_0$. Several patterns of streaming can be generated depending on the value of the ratio y_0/δ_ν namely, Rayleigh-type streaming in the central region and boundary layer type streaming near the longitudinal walls of the enclosure. Isothermal no-slip physical boundary conditions are employed in the solid walls of the moving frame.

3. Numerical methodology

We discretize the governing equations using high-order (formally greater or equal to fourth-order) accurate numerical schemes in both space and time. The proposed numerical solver utilizes high-order compact schemes along each spatial dimension, formulated on a collocated grid arrangement. The chosen temporal discretization is carried out by a fourth-order Runge-Kutta (RK4) method. Compact (or Padé) schemes are attractive since they allow the use of relatively small finite difference stencils to gain high-order accuracy. In general, they allow better resolution at higher wave numbers and offer the potential of spectral-type accuracy but with greater geometrical flexibility [27]. Although high-order accuracy can be obtained also by classical explicit finite difference formulas, the obtained formulas in the classical approach lead to wider stencils and hence the non-compact form of the difference scheme is less convenient, especially close to the boundaries.

3.1. Higher-order spatial and temporal discretizations

Assuming a non-uniform discretization at each spatial direction, the enclosure's physical domain $\Omega \equiv [0, L] \times [0, 2y_0] = [0, L] \times [0, H]$ is subdivided into cells of width Δx and height Δy in the $x-$ and $y-$direction, respectively, with $\Delta x = L/(N_x - 1)$ and $\Delta y = H/(N_y - 1)$ where N_x and N_y are the numbers of mesh points in each direction. The vertices of each computational cell are denoted as (x_i, y_j), with $x_i = (i-1)\Delta x$ and $y_j = (j-1)\Delta y$ for $1 \le i \le N_x$ and $1 \le j \le N_y$. The mesh points denoted by the indices $i = 1$, $i = N_x$, $j = 1$ and $j = N_y$ are boundary nodes, lying on the boundary of the physical domain

Ω. The collocation arrangement of the grid variables is adopted in which all flow-field variables are evaluated at the same set of nodal points.

3.1.1. Spatial Discretization

Compact, Padé-type finite difference schemes [27, 37], are used to obtain high-order accuracy for the derivatives of the inviscid $\mathbf{F}, \mathbf{G}$ and viscous $\mathbf{F}_\nu, \mathbf{G}_\nu$ fluxes. Compact schemes evaluate the derivatives in a coupled fashion by solving tridiagonal linear systems.
Discretization of the second-order derivatives in the viscous fluxes $\mathbf{F}_\nu$ and $\mathbf{G}_\nu$ on collocated grids are derived by the application of the first derivative approximation twice. We shall now derive a high-order compact scheme for the first spatial derivatives in the model Eq. (2). For the implementation, it is necessary to impose boundary conditions to obtain closed systems. In particular, for a collocated uniform infinite grid

$$\mathbf{G}_{\boldsymbol{h}} := \{(x, y) : x = x_i = (i-1)\Delta x,\ y = y_j = (j-1)\Delta y;\ i, j \in \mathbb{Z}\}\ . \qquad (10)$$

with $\boldsymbol{h} = (\Delta x, \Delta y)$ the vector of fixed mesh sizes, we define $\Omega_h := \Omega \cap \mathbf{G}_h$.

As proposed in [27], and in one-dimension, the first derivative's value ϕ'_i on an interior mesh points x_i of a generic function $\phi(x)$ (assuming for convenience that $\boldsymbol{h} = h = \Delta x$) can be approximated in a coupled fashion with the centered formula as

$$\begin{aligned} &\beta\phi'_{i-2} + \alpha\phi'_{i-1} + \phi'_i + \alpha\phi'_{i+1} + \beta\phi'_{i+2} = \\ &= c\frac{\phi_{i+3} - \phi_{i-3}}{6h} + b\frac{\phi_{i+2} - \phi_{i-2}}{4h} + a\frac{\phi_{i+1} - \phi_{i-1}}{2h}. \end{aligned} \qquad (11)$$

For at least fourth-order accuracy the constraints for the coefficients satisfy the equations

$$a + b + c = 1 + 2\alpha + 2\beta, \quad a + 2^2 b + 3^2 c = 2\frac{3!}{2!}(\alpha + 2^2\beta). \qquad (12)$$

and the corresponding truncation error on the right-hand side of (11) is

$$\frac{4}{5!}(-1 + 3\alpha - 12\beta + 10c)h^4\phi^{(5)}.$$

Choosing $\beta = 0$ and $c = 0$, a one-parameter family of fourth-order schemes, in tridiagonal form, can be obtained. Further, if one chooses $\alpha = \dfrac{1}{3}$ the leading order of the truncation error coefficient vanishes and the scheme is formally of sixth-order accuracy.

To maintain the tridiagonal nature of the above scheme, the formula employed at a point close to the boundary is given as

$$\phi_1' + \tilde{\alpha}\phi_2' = \frac{1}{h}(\tilde{a}\phi_1 + \tilde{b}\phi_2 + \tilde{c}\phi_3 + \tilde{d}\phi_4). \tag{13}$$

Requiring (13) to be at least third-order accurate constrains the coefficients to

$$\tilde{a} = -\frac{11 + 2\tilde{\alpha}}{6}, \quad \tilde{b} = \frac{6 - \tilde{\alpha}}{2}, \quad \tilde{c} = \frac{2\tilde{\alpha} - 3}{2}, \quad \tilde{d} = \frac{2 - \tilde{\alpha}}{6} \tag{14}$$

and the corresponding truncation error on the right-hand side of (11) is

$$(2(\tilde{\alpha} - 3)/4!)h^3\phi_1^{(4)}.$$

If one chooses $\tilde{\alpha} = 3$ the leading order of the truncation error coefficient vanishes and the scheme is formally of fourth-order accuracy. It may be noted that, for $\tilde{\alpha} \neq 3$ the leading order truncation error is of dissipative type, while for $\tilde{\alpha} = 3$ is of a dispersive type. An investigation of different boundary closures (based on the parameter $\tilde{\alpha}$) is necessary to avoid a reduction of the formal order-of-accuracy of the numerical scheme or/and ensure a stable numerical scheme.

In a 2D generic representation of the spatial discretization, the first-order derivatives along the x-direction of a general differentiable function $\phi(x, y)$, are computed in a coupled fashion assuming grid function values of ϕ and $\phi^{'}$, denoted as $\phi_{i,j}$ and $\phi^{'}_{i,j}$ respectively, at mesh points (x_i, y_j), $i = 1, ..., N_x$, by solving the following N_y linear systems

$$\mathcal{P}_x\phi'_{i,j} = \mathcal{Q}_x\phi_{i,j}, \quad j = 1, ..., N_y, \tag{15}$$

with the compact finite-difference operators $\mathcal{P}_x$ and $\mathcal{Q}_x$ defined as

$$\mathcal{P}_x\phi^{'}_{i,j} = \begin{cases} \phi^{'}_{1,j} + \tilde{\alpha}\phi^{'}_{2,j}\ , & i = 1; \\ \phi^{'}_{1,j} + 4\phi^{'}_{2,j} + \phi^{'}_{3,j} & i = 2; \\ \phi^{'}_{i-1,j} + 3\phi^{'}_{i,j} + \phi^{'}_{i+1,j}\ , & i = 3, ..., N_x - 2; \\ \phi^{'}_{N_x-2,j} + 4\phi^{'}_{N_x-1,j} + \phi^{'}_{N_x,j} & i = N_x - 1; \\ \tilde{\alpha}\phi^{'}_{N_x-1,j} + \phi^{'}_{N_x,j}, & i = N_x, \end{cases} \tag{16}$$

and

$$\mathcal{Q}_x\phi_{i,j} = \begin{cases} \dfrac{1}{2h}(\tilde{a}\phi_{1,j} + \tilde{b}\phi_{2,j} + \tilde{c}\phi_{3,j} + \tilde{d}\phi_{4,j}), & i = 1; \\ \dfrac{3}{h}(\phi_{3,j} - \phi_{1,j}), & i = 2; \\ \dfrac{1}{12h}\left(28(\phi_{i+1,j} - \phi_{i-1,j}) + \phi_{i+2,j} - \phi_{i-2,j}\right), & i = 3, ..., N_x - 2; \\ \dfrac{3}{h}(\phi_{N_x,j} - \phi_{N_x-2,j}), & i = N_x - 1; \\ \dfrac{1}{2h}(\tilde{d}\phi_{N_x-3,j} + \tilde{c}\phi_{N_x-2,j} + \tilde{b}\phi_{N_x-1,j} + \tilde{a}\phi_{N_x,j}),\ , & i = N_x. \end{cases} \tag{17}$$

It follows that with the above representation we can define the linear space of all grid functions, that act on Ω_h, by $\mathcal{G}(\Omega_h)$. Thus, $\mathcal{P}_x$ and $\mathcal{Q}_x$ are the linear operators along the x-direction

$$\mathcal{P}_x, \mathcal{Q}_x : \mathcal{G}(\Omega_h) \to \mathcal{G}(\Omega_h). \tag{18}$$

Similarly we can define the linear operators along the $y-$direction as $\mathcal{P}_y$ and $\mathcal{Q}_y$ by interchanging the i and j indices accordingly.

The above results in a complete fourth-order first derivative approximation scheme obtained with compact formulas which can be written in an abbreviated form as C3-4-6-4-3 for $\tilde{\alpha} \neq 3$ and C4-4-6-4-4 for $\tilde{\alpha} = 3$. The first and last numbers in the abbreviation denote the order of accuracy of the scheme on the boundary nodes, while the second and before last numbers denote the order of the near boundary nodes, and the central number represents the order of the inner approximation. As shown in [27], using eigenvalue analysis, for the one-dimensional advection equation, the differencing scheme (15) for $\tilde{\alpha} = 2$ generates a numerically stable algorithm. This was also the case in our simulations in this work, since using scheme C4-4-6-4-4 and for various values of $\tilde{\alpha}$ wasn't able to provide stable solutions in all cases. Thus, scheme C3-4-6-4-3 with $\tilde{\alpha} = 2$ was implemented throughout the current presentation. The second-order derivatives are computed with the successive application of (15) twice, which retains the order of accuracy.

Now, Eq. (2) can be written in the following semi-discrete compact form:

$$\frac{\mathrm{d}\mathbf{U}_{i,j}}{\mathrm{d}t} = \mathbf{R}(\mathbf{U}_{i,j}; t) \tag{19}$$

where the discretized components of the right-hand side vector of Eq. (19) are given (omitting for clarity the i, j indices) by

$$R_1(\mathbf{U}; t) = -\mathcal{P}_x^{-1}\mathcal{Q}_x(\rho u) - \mathcal{P}_y^{-1}\mathcal{Q}_y(\rho v), \tag{20}$$

$$R_2(\mathbf{U}; t) = \mathcal{P}_x^{-1}\mathcal{Q}_x\left(\mathcal{T}_{xx}\mathbf{u} - \rho u^2 - p\right) + \mathcal{P}_y^{-1}\mathcal{Q}_y\left(\mathcal{T}_{xy}\mathbf{u} - \rho uv\right) - \rho\frac{\mathrm{d}V}{\mathrm{d}t}, \tag{21}$$

.

$$R_3(\mathbf{U}; t) = \mathcal{P}_x^{-1}\mathcal{Q}_x\left(\mathcal{T}_{xy}\mathbf{u} - \rho uv\right) + \mathcal{P}_y^{-1}\mathcal{Q}_y\left(\mathcal{T}_{yy}\mathbf{u} - \rho v^2 - p\right). \tag{22}$$

$$\begin{aligned} R_4(\mathbf{U}; t) = {} & \mathcal{P}_x^{-1}\mathcal{Q}_x\left(u\mathcal{T}_{xx}\mathbf{u} + v\mathcal{T}_{xy}\mathbf{u} - \rho E u - pu + k\mathcal{P}_x^{-1}\mathcal{Q}_x T\right) + \\ & \mathcal{P}_y^{-1}\mathcal{Q}_y\left(u\mathcal{T}_{xy}\mathbf{u} + v\mathcal{T}_{yy}\mathbf{u} - \rho E v - pv + k\mathcal{P}_y^{-1}\mathcal{Q}_y T\right) - \rho u\frac{\mathrm{d}V}{\mathrm{d}t} \end{aligned} \tag{23}$$

where the discrete operators $\mathcal{T}_{yy}$, $\mathcal{T}_{yy}$ and $\mathcal{T}_{xy}$ are given by

$$\mathcal{T}_{xx}\mathbf{u} = \frac{4}{3}\mu\mathcal{P}_x^{-1}\mathcal{Q}_x u - \frac{2}{3}\mu\mathcal{P}_y^{-1}\mathcal{Q}_y v \tag{24}$$

$$\mathcal{T}_{yy}\mathbf{u} = \frac{4}{3}\mu\mathcal{P}_y^{-1}\mathcal{Q}_y v - \frac{2}{3}\mu\mathcal{P}_x^{-1}\mathcal{Q}_x u \tag{25}$$

$$\mathcal{T}_{xy}\mathbf{u} = \mu\left(\mathcal{P}_y^{-1}\mathcal{Q}_y u + \mathcal{P}_x^{-1}\mathcal{Q}_x v\right) \tag{26}$$

with $\mathbf{u} = [u, v]^{\mathrm{T}}$.

3.2. Temporal Discretization

An explicit Runge-Kutta scheme with fourth-order accuracy is employed for the temporal discretization of Eq. (19),

$$\mathbf{U}^{n,1} = \mathbf{U}^n, \qquad \mathbf{p}^{n,1} = \mathbf{p}^n, \mathbf{P}^{n,1} = \mathbf{T}^n, \tag{27}$$

$$\mathbf{U}^{n,2} = \mathbf{U}^n + \frac{\Delta t}{2}\mathbf{R}^{n,1}, \quad \mathbf{p}^{n,2}, \mathbf{T}^{n,2} \quad \textit{from Eqs. (8), (9)} \tag{28}$$

$$\mathbf{U}^{n,3} = \mathbf{U}^n + \frac{\Delta t}{2}\mathbf{R}^{n,2} \quad \mathbf{p}^{n,3}, \mathbf{T}^{n,3} \quad \textit{from Eqs. (8), (9)} \tag{29}$$

$$\mathbf{U}^{n,4} = \mathbf{U}^n + \Delta t\mathbf{R}^{n,3}, \quad \mathbf{p}^{n,4}, \mathbf{T}^{n,4} \quad \textit{from Eqs. (8), (9)} \tag{30}$$

$$\mathbf{U}^{n+1} = \mathbf{U}^n + \frac{\Delta t}{6}\left(\mathbf{R}^{n,1} + 2\mathbf{R}^{n,2} + 2\mathbf{R}^{n,3} + \mathbf{R}^{n,4}\right), \quad \mathbf{p}^{n+1}, \mathbf{T}^{n+1} \quad \textit{from Eqs. (8), (9)} \tag{31}$$

with $t^n = n\Delta t$, $t^{n,1} = t^n$, $t^{n,2} = t^{n,3} = t^n + \Delta t/2$, $t^{n,4} = t^n + \Delta t$, and $\mathbf{R}^{n,\ell} = \mathbf{R}(\mathbf{U}^{n,\ell}; t^{n,\ell})$, for $\ell = 2, 3, 4$.

For the RK4 scheme, being fully explicit, the time step Δt is fixed to satisfy its stability condition. In all cases considered next, the time step limitation is acoustic, and it is given by

$$\Delta t \leq \mathrm{CFL} \cdot \frac{h_{\min}}{c_0}, \quad h_{\min} = \min(\Delta x, \Delta y) \tag{32}$$

where the CFL number is less than one. In all the simulations presented in the next section the CFL number was set to 0.5, unless otherwise stated.

3.3. Boundary Conditions

As stated before, isothermal and no-slip boundary conditions were imposed for all walls. Hence, for the velocities and temperature along the boundaries we impose

$$u(0, y, t) = v(0, y, t) = 0, \quad u(L, y, t) = v(L, y, t) = 0,$$

$$u(x, 0, t) = v(x, 0, t) = 0, \quad u(x, H, t) = v(x, H, t) = 0,$$

$$T(0, y, t) = T(L, y, t) = T(x, 0, t) = T(x, H, t) = T_0.$$

The spectral-like differencing scheme proposed here, requires accurate boundary conditions. To this end, the characteristic boundary conditions for the Navier-Stokes equations where implemented for the density, adapted from [38]. This procedure is based on the characteristic wave theory and avoids numerical instabilities while controlling spurious wave reflections at the computational boundaries. Specifically we solve

$$\frac{\partial \rho(x,0)}{\partial t} = \frac{1}{c}\frac{\partial p(x,0)}{\partial y} - \rho(x,0)\frac{\partial v(x,0)}{\partial y}, \tag{33}$$

$$\frac{\partial \rho(x,H)}{\partial t} = -\frac{1}{c}\frac{\partial p(x,H)}{\partial y} - \rho(x,H)\frac{\partial v(x,H)}{\partial y}, \tag{34}$$

$$\frac{\partial \rho(0,y)}{\partial t} = \frac{1}{c}\frac{\partial p(0,y)}{\partial x} - \rho(0,y)\frac{\partial u(0,y)}{\partial x}, \tag{35}$$

$$\frac{\partial \rho(L,y)}{\partial t} = -\frac{1}{c}\frac{\partial p(L,y)}{\partial x} - \rho(L,y)\frac{\partial u(L,y)}{\partial x}. \tag{36}$$

For the boundary nodes, where eqs (33)-(36) apply, the relevant spatial derivatives are simply computed using the values that have been obtained from the formulas in (16) and (17) for $i = 1$ and $i = N_x$ and from the resulting system (15). Similar for the y-direction. Further, at the end of each step of the Runge-Kutta method the pressure and the energy at the boundaries are calculated from

$$p = \rho R T_0 \quad \text{and} \quad E = \frac{RT_0}{\gamma - 1}. \tag{37}$$

3.4. Numerical Filtering

Compact-difference discretizations, like other centered schemes, are nondissipative and are therefore susceptible to numerical instabilities due to the growth of high-frequency modes. These difficulties may originate mainly from mesh non-uniformity, boundary conditions, and highly nonlinear flow features. Since traveling shock-like waves are present for flows of high acoustics levels, a high-order implicit filtering technique [31, 39] is incorporated to alleviate the spurious oscillations arising from instabilities.

If a component of the obtained (from the core numerical scheme) discretized solution vector is denoted by $\phi_{i,j}$, filtered values $\hat{\phi}_{i,j}$, e.g in $x-$direction, are obtained by solving the following N_y linear systems

$$\mathcal{P}_f \hat{\phi}_{i,j} = \mathcal{Q}_f \phi_{i,j}, \qquad j = 1, ..., N_y \tag{38}$$

with the compact finite-difference operators $\mathcal{P}_f$ and $\mathcal{Q}_f$ defined as

$$\mathcal{P}_f \hat{\phi}_{i,j} = \begin{cases} \hat{\phi}_{1,j} & i = 1; \\ \alpha_f \hat{\phi}_{1,j} + \hat{\phi}_{2,j} + \alpha_f \hat{\phi}_{3,j} & i = 2, ..., K; \\ \alpha_f \hat{\phi}_{i-1,j} + \hat{\phi}_{i,j} + \alpha_f \hat{\phi}_{i+1,j} & i = K+1, ..., N_x - K; \\ \alpha_f \hat{\phi}_{N_x-k,j} + \hat{\phi}'_{N_x-k+1,j} + \alpha_f \hat{\phi}_{N_x-k+2,j} & i = N_x - K + 1, ..., N_x - 1; \\ \hat{\phi}_{N_x,j} & i = N_x, \end{cases} \tag{39}$$

and

$$\mathcal{Q}_f \phi_{i,j} = \begin{cases} \phi_{1,j} & i = 1; \\ \displaystyle\sum_{n=1}^{K+1} a_{n,i} \phi_{n,j} & i = 2, ..., K; \\ \displaystyle\sum_{n=0}^{K} \frac{a_n}{2} (\phi_{i+n,j} + \phi_{i-n,j}) & i = K+1, ..., N_x - K; \\ \displaystyle\sum_{n=1}^{K+1} a_{n,i-N_x+K+1} \phi_{N_x-n+1,j} & i = N_x - K + 1, ..., N_x - 1; \\ \phi_{N_x,j}\ , & i = N_x \end{cases} \tag{40}$$

System (38) provides a $2K$th-order accurate (OA) formula on a $2K+1$ point stencil. Based on coefficient values proposed in [27, 31], the $K+1$ coefficients, $a_0, a_1, \ldots a_K$ and coefficients $a_{1,i}, a_{2,i}, \ldots a_{K+1,i}$ for $i = 2, .., K$, are derived in terms of an adjustable α_f with Taylor- and Fourier-series analysis. These are presented in Tables 5-7 in the Appendix. Further, in [31] spectral responses of these filters were analyzed. The adjustable parameter α_f should satisfy the restriction $-0.5 < \alpha_f \leq 0.5$, with higher values of α_f corresponding to a less dissipative filtering. Extensive numerical experience suggests that regardless of the time-integration scheme, values of α_f between 0.3 and 0.5 are appropriate. In general, the filter is typically chosen to be at least two orders of accuracy higher than the compact difference scheme.

We note here that, the filtering process is not applied at the boundary nodes. Tables 6 and 7 in the Appendix list coefficients for the higher-order one-sided boundary filter formulas that can be employed at discrete points near the boundary when the filter is used for the interior points can not be applied due to stencil restrictions. An extensive listing of boundary filter coefficients is provided in [37]. In the present work, the solution is filtered once after the final stage of the explicit Runge-Kutta method. When shock-like waves occur, the proposed high-order numerical scheme is coupled with such a filter scheme to achieve convergence (for steady-state solutions). In this work, filtering is applied to the conserved variables and four different strategies have been investigated for its application, as to recognize the most efficient one, (a) sequentially in each coordinate direction, (b) in the x-direction only, (c) in the y-direction only and (d) along the physical direction of the filtered conserved variables i.e. along the $x-$direction for the variables $\rho, \rho u, \rho E$ and along the y-direction for the ρv variable. To this end, the core numerical scheme C3-4-6-4-3 from Section 3.1.1 can be combined with different filtering options resulting in an overall stable high-order numerical solver. We can abbreviate the filtering (F) combination used as, for example, F(b):B6-B6-I6-B6-B6$^{0.45}$ for filtering in the x-direction only (option (b) from above), with $\alpha_f = 0.45$, when a 6th-order filter is chosen in the second and third discrete layers from the boundary (B) as well as at the rest interior (I) discrete points.

Remark 1. In general, for cases of slow streaming i.e. $Re_{NL} \ll 1$, no filtering need to be applied. For cases of $Re_{NL} = O(1)$ solutions converged to a steady state but spurious oscillations appeared in the solution. For higher Re_{NL} cases and strongly nonlinear streaming regimes, filtering was mandatory. To this end, various filtering combinations were tested during this work, for the different cases presented below, to conclude to the most accurate and robust one combined with the core scheme C3-4-6-4-3. In terms of the different filtering strategies (a)-(b) above it was found that for $Re_{NL} \leq 4$ option (b) was sufficient while for higher Re_{NL} numbers option (d) was proven the most accurate. In terms of the order of filtering used at the two layers of grid points near the boundary, applying 6th-order filtering was proven to be the most accurate and robust for flows with moderate Re_{NL} numbers.

4. Numerical tests and results

In this section we present numerical tests and results to verify the ability of the proposed numerical scheme (and its variations) to simulate the generated streaming patterns as well as to detail its proper implementation (in terms of boundary closure formulas and filtering options). We assume an enclosure initially filled with air with uniform values for pressure $p_0 = 101325 Pa$, density $\rho_0 = 1.2 kg/m^3$ and temperature $T_0 = 294.15 K$. The thermo-physical properties for air are $\mu = 1.795 \cdot 10^{-5} kg/(ms)$, $k = 0.025 W/(mK)$, $\gamma = 1.4$ and $R = 287.06 J/(kgK)$. The resulting initial speed of sound is $c_0 = 343.82 m/s$ with the Prandtl number $Pr = 0.7213$.

In the harmonic velocity law, the vibration frequency of the enclosure is set to $f = 20000 Hz$, which corresponds to a high-frequency wave. The resulting wavelength of the sound waves at this frequency is $\lambda = 17.191 mm$ for the resulting value of c_0. The length of the enclosure is chosen to be $L = \lambda/2 = 8.5955 mm$ and the resulting acoustic boundary layer thickness is $\delta_\nu = 1.543 \cdot 10^{-2} mm$. The acoustic velocity produced in the enclosure depends on the ratio y_0/δ_ν, varying from a narrow geometry to wider enclosures, and on the amplitude $x_{\max}$ of the displacement in the harmonic velocity law. These parameters for the test cases considered in this work are given in Table 1.

For all numerical simulations performed, and as stated before, a Cartesian mesh of rectangular cells of constant size $\Delta x \times \Delta y$ was implemented, with $\Delta x = L/(N_x - 1)$ and $\Delta y = H/(N_y - 1)$ being the spatial discretization lengths in the x and $y-$direction, respectively, where N_x and N_y are the mesh points used. Here, we have used $N_x = 501$ mesh points in the $x-$direction, in most cases, and in order to obtain at least five points per boundary layer thickness we set $\Delta y = \delta_\nu/5$ [13].

Table 1: Simulations test cases: parameters used (top half of table) and resulted characteristic values (bottom half)

Parameters	**Case 0**	**Case 1**	**Case 2**	**Case 3**	**Case 4**	**Case 5**	**Case 6**
$x_{\max}(\mu m)$	5	5	80	10	50	100	35
y_0/δ_ν	6	10	10	40	20	20	60
H/L	0.0215	0.0359	0.0359	0.1436	0.0718	0.0718	0.2154
$N_x \times N_y$	501×61	501×101	501×101	501×401	501×201	601×241	301×601
$\widehat{U}_{\max}(m/s)$	4.748	7.724	71.52	26.35	61.32	90.38	63.60
M	0.013	0.022	0.208	0.076	0.178	0.2628	0.1849
Re_S	11.99	31.73	2721.20	369.60	1666.97	4345.62	2151.76
Re_{NL}	0.0068	0.0504	4.327	9.403	12.723	27.640	123.17

As referenced in the Introduction, the regularity of the streaming flow is described by the nonlinear Reynolds number Re_{NL}. In this work, and for comparison purposes, the definition of $Re_{NL} = (\widehat{U}_{\max}/c_0 \times y_0/\delta\nu)^2 = (M \times y_0/\delta\nu)^2$ is that of [13] which corresponds to half of that of Menguy and Gilbert [6]. In the simulations performed here, several Re_{NL} values are considered ranging from very slow streaming flow ($Re_{NL} = 0.0068$) to fast streaming flow (Re_{NL}=27.640) and also a case with $Re_{NL} = 123.17$, for several values of the ratio y_0/δ_ν and for Mach numbers ranging from $M = 0.013$ to $M = 0.26$ as shown in Table 1. Another dimensionless parameter that is frequently used in the study of streaming flows is the streaming Reynolds number which can be defined in terms of the maximum acoustic velocity as $Re_S = \widehat{U}^2_{\max}/\nu\omega$, [21, 10], and has been included here for comparison purposes. The relation between these two dimensionless parameters is $Re_S = \dfrac{\lambda^2}{2\pi^2 y_0^2} Re_{NL}$. We also note here that $\widehat{U}_{\max}$ is defined to be the maximum amplitude of $U_{\max}$ which is defined here, and in the following, as the acoustic velocity amplitude at the velocity antinode.

4.1. Case 0

In this case, the enclosure half-width is the smallest one and, given the value of the resulting Re_{NL}, the problem is almost linear. Thus, this test case aims to compare the numerical results, obtained with the core compact scheme C3-4-6-4-3, with those obtained with linear theory as well as its numerical accuracy.

Figure 2 presents the velocity signal (denoted here as $U_{\max}$) at the center of the enclosure and pressure variation, denoted here as $p_{\max}$, at the enclosure's end as functions of the number of periods. The center of the enclosure corresponds to an antinode thus the acoustic velocity gets its maximum at this point. The periodic regime established after about 10 periods can be seen. The final signal is purely sinusoidal, in agreement with the linear theory.

Figure 3 presents the velocity and pressure distributions along the symmetry of the $y-$axis in the enclosure, up to the 20th period. The primary oscillatory flow is periodic and at $\omega t = \pi/2$ and $\omega t = 3\pi/2$, the velocity's maximum and minimum values are obtained. At the beginning of the period cycle, the pressure

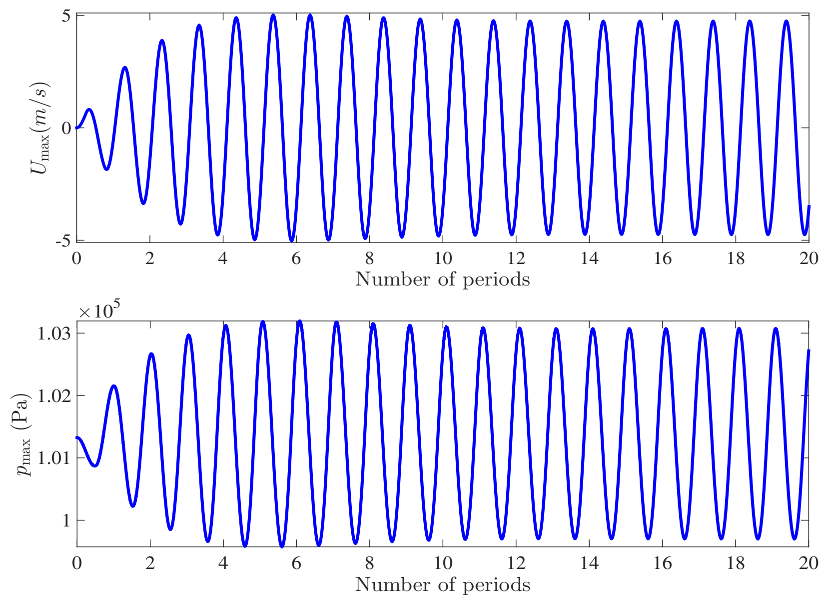

Figure 2: Case 0: Acoustic velocity (top) at the center of the enclosure and pressure (bottom) at the of the enclosure at $x = L$, as functions of the number of periods elapsed

is maximum at the left wall, decreasing with distance reaching a minimum at $x = L$. At $\omega t = \pi$ the pressure profile is symmetric to the profile given at $\omega t = 0$ concerning the vertical mid-plane, reaching a maximum at the right wall. The presented pressure profiles intersect at $x = L/2$ creating a pressure node. The perfect sinusoidal profile of the emitted wave by the oscillating enclosure is very slightly distorted due to the nonlinear effects.

Further, in Figure 4 streamlines of the mean flow field are shown. This flow field is computed by time average quantities over an acoustic period (the 20th in our case) and the mean velocity values u^M and v^M, also called Eulerian streaming velocities, are obtained. In this case, four clockwise and four counterclockwise circulations (vortical structures) can be observed. Four of these vortical structures (called inner streaming) are formed in the vicinity of the horizontal walls and their height defines the thickness of the acoustic boundary layer. The four vortical structures in the middle section of the enclosure define

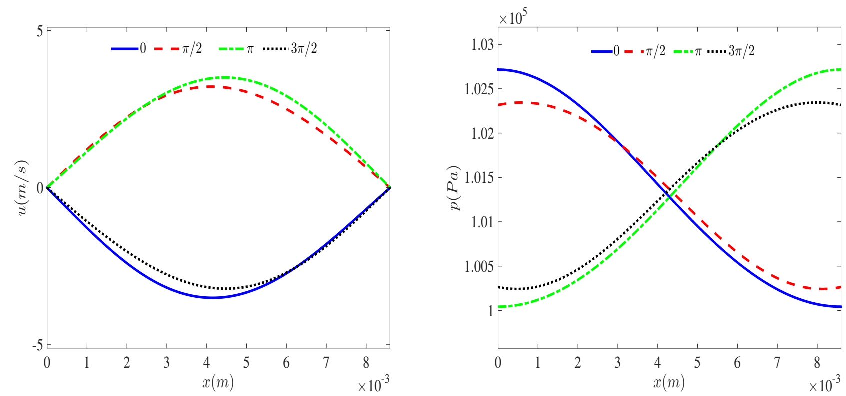

Figure 3: Case 0: Variation of the u velocity (left) and pressure (right) along the symmetry of $y-$axis at $\omega t = 0, \pi/2, \pi, 3\pi/2$

the so-called outer streaming. The horizontal length of both the outer and inner streaming vortices is characterized by a quarter-wavelength. Further, the analytical solution of [8] for the streamlines at the upper quarter of the enclosure is given, verifying the accuracy of the numerical results. It is noted that the exact solution in [8] is obtained by imposing the harmonic excitation to an enclosure of infinite length.

Figure 5 shows the variation of the computed dimensionless streaming velocity for the u component at $x = 3L/4$ and for the v component at $x = L/2$ using as as reference velocity the Rayleigh streaming velocity defined as $u_R = 3\widehat{U}^2_{\max}/16c_0$ [7, 8, 21, 13]. Again, numerical results are compared with the analytical solution of [8] and a perfect agreement can be observed.

Finally, for this preliminary test case, the obtained mean temperature field is shown in Figure 6. As expected, for very small Re_{NL} numbers the mean temperature difference inside the enclosure is very small leading to a negligible mean temperature gradient (difference between the minimum and maximum values of temperature) of value $\Delta T \approx 0.02K$.

To obtain a numerical accuracy indication of the proposed numerical scheme C3-4-6-4-3, a convergence study is presented next. Using a numerical reference solution obtained with a fine mesh of $N_x = 2000$ mesh points, the rate of

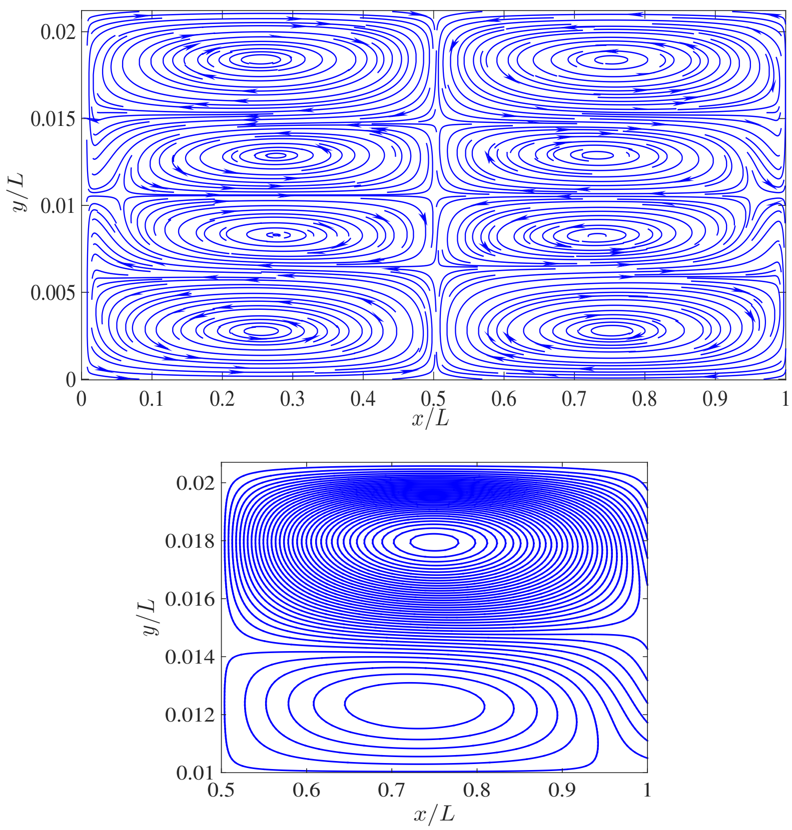

Figure 4: Case 0: streamlines of the numerical mean flow along the enclosure (top) and analytical streamlines for the upper right quarter from [8] (bottom)

convergence, r, in all usual norms are given in Tables 2 and 3 for the velocities u and v. As it can be observed the numerical scheme reaches the expected formal order of accuracy.

4.2. Case 1

The problem for this case is nearly linear and has also been considered in [13]. Again the core compact scheme C3-4-6-4-3 has been applied. Figure 7 presents the velocity signal and pressure variation at the center and at the end of the enclosure, respectively, as functions of the number of periods. The amplification

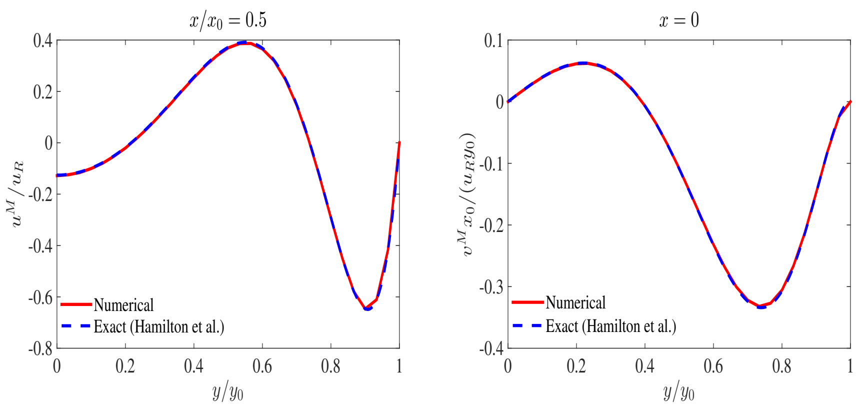

Figure 5: Case 0: Variation of the computed streaming velocity as a function of y/y_0 for the u^M component at $x = 3L/4$ (left) and for the v^M component at $x = L/2$ (right)

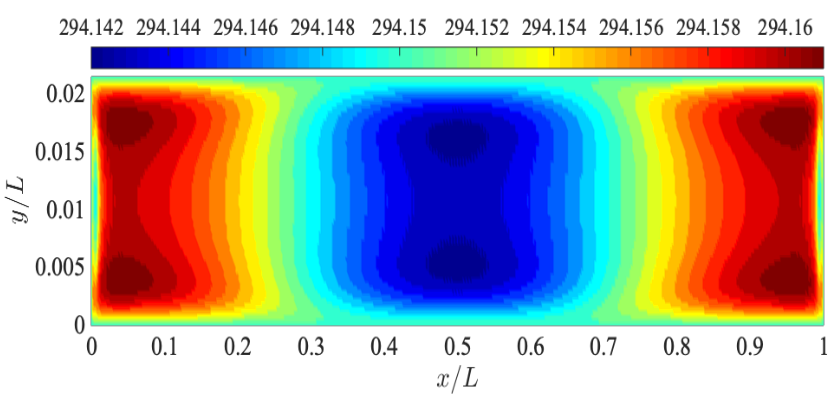

Figure 6: Case 0: mean temperature field along the enclosure

of the initial perturbation and the subsequent periodic regime established after about 20 periods can be seen.

Figure 8 presents the velocity and pressure distributions along the symmetry of the $y-$axis in the enclosure, during the 100th period. The primary oscillatory flow is again periodic and at $\omega t = \pi/2$ and $\omega t = 3\pi/2$, the velocity's maximum and minimum values are obtained. At the beginning of the period cycle, the pressure is maximum at the left wall, decreasing with distance reaching a minimum at $x = L$. At $\omega t = \pi$ the pressure profile is fairly symmetric to the profile

Table 2: Case 0: Numerical convergence rates (r) for the velocity u

N_x	$E(L^1)$	r	$E(L^2)$	r	$E(L^\infty)$	r
125	$2.450 \cdot 10^{-2}$	-	$2.805 \cdot 10^{-2}$	-	$3.746 \cdot 10^{-2}$	-
250	$1.221 \cdot 10^{-2}$	1.01	$1.367 \cdot 10^{-2}$	1.04	$1.982 \cdot 10^{-2}$	0.92
500	$2.650 \cdot 10^{-3}$	2.21	$3.052 \cdot 10^{-3}$	2.16	$4.622 \cdot 10^{-3}$	2.10
1000	$1.335 \cdot 10^{-4}$	4.31	$1.588 \cdot 10^{-4}$	4.27	$2.861 \cdot 10^{-4}$	4.01

Table 3: Case 0: Numerical convergence rates (r) for the velocity v

N_x	$E(L^1)$	r	$E(L^2)$	r	$E(L^\infty)$	r
125	$1.122 \cdot 10^{-5}$	-	$1.556 \cdot 10^{-5}$	-	$3.081 \cdot 10^{-5}$	-
250	$5.119 \cdot 10^{-6}$	1.13	$6.578 \cdot 10^{-6}$	1.24	$1.216 \cdot 10^{-5}$	1.34
500	$1.121 \cdot 10^{-6}$	2.19	$1.551 \cdot 10^{-6}$	2.15	$2.878 \cdot 10^{-6}$	2.08
1000	$7.786 \cdot 10^{-8}$	3.95	$1.021 \cdot 10^{-7}$	3.93	$2.010 \cdot 10^{-7}$	3.84

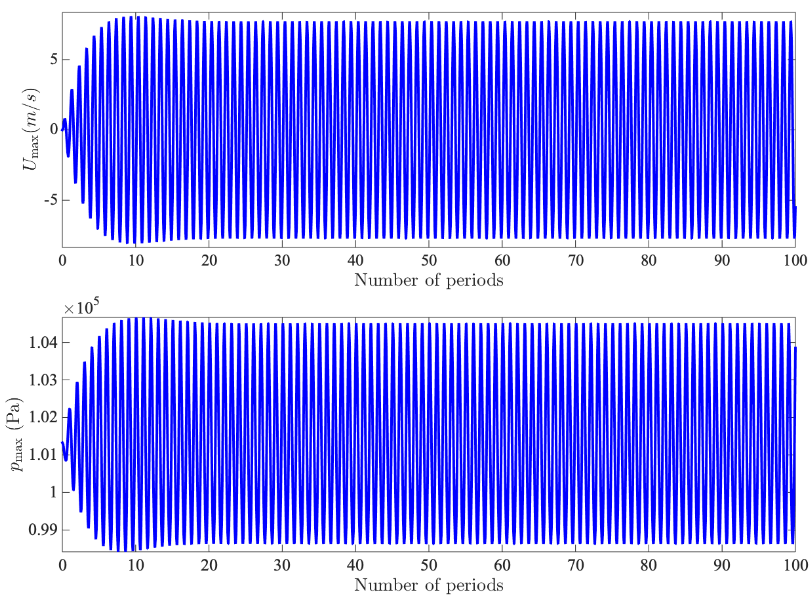

Figure 7: Case 1: Acoustic velocity (top) at the center of the enclosure and pressure (bottom) at the of the enclosure at $x = L$, as functions of the number of periods elapsed

given at $\omega t = 0$, concerning the vertical mid-plane, reaching a maximum at the right wall. The presented pressure profiles intersect around $x = L/2$ while due to attenuation caused by viscous and nonlinear effects, both pressure and velocity profiles slightly differ from a perfect sinusoidal wave field.

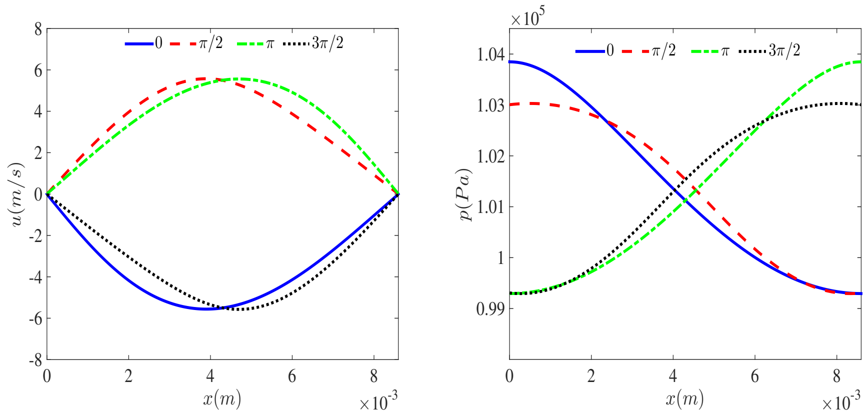

Figure 8: Case 1: Variation of the u velocity (left) and pressure along the symmetry axis at $\omega t = 0, \pi/2, \pi, 3\pi/2$

Further, in Figure 9 streamlines of the mean flow field are shown along with the analytical field obtained from the analytical solution of [8]. The so-called Rayleigh streaming can be identified with four symmetric streaming cells developed over the length and half-width of the enclosure; two cells in the boundary layers (inner streaming) and two cells in the core of the enclosure (outer streaming). These results are in agreement with those obtained by analytical and numerical models of streaming flows [7, 8, 26, 13] as well as with experimental measurements [40]. The maximum streaming velocity, u^M, value is found to be approximately $0.028 m/s$ in this case. To this end, Figure 10 shows the variation of the computed dimensionless streaming velocity for the u^M component at $x = 3L/4$ and for the v^M component at $x = L/2$. Again, the numerical results of the current study are compared with the analytical solution of [8] and an almost perfect agreement can be observed. It is noted here that the results presented for this test case are more accurate when compared to the analytical solution than those presented in [13].

Finally, for Case 1, the obtained mean temperature field is shown in Figure 11. Similar to Case 0 for very small Re_{NL} numbers the mean temperature difference inside the enclosure is very small ($\Delta T \approx 0.05K$) leading to a negligible mean temperature gradient. However, as shown experimentally in [25] and

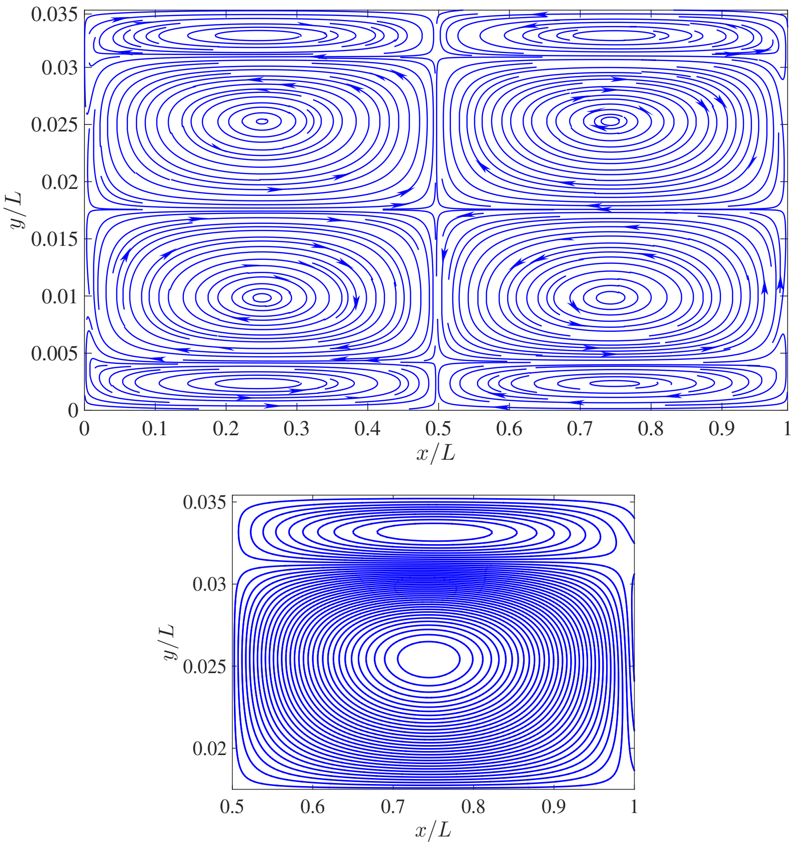

Figure 9: Case 1: streamlines of the numerical mean flow along the enclosure (top) and analytical streamlines for the upper right quarter from [8]

verified numerically in [13], this mean temperature gradient established inside the enclosure results from the heat that is removed from velocity antinodes, i.e. at the location of largest viscous dissipation, and the heat that is produced along the lateral wall i.e. close to velocity nodes. Thus, the thermoacoustic heat transport takes place at a distance of one thermal boundary layer thickness and then heat diffuses, resulting in a temperature field that is almost one-dimensional in the central part of the enclosure at steady state.

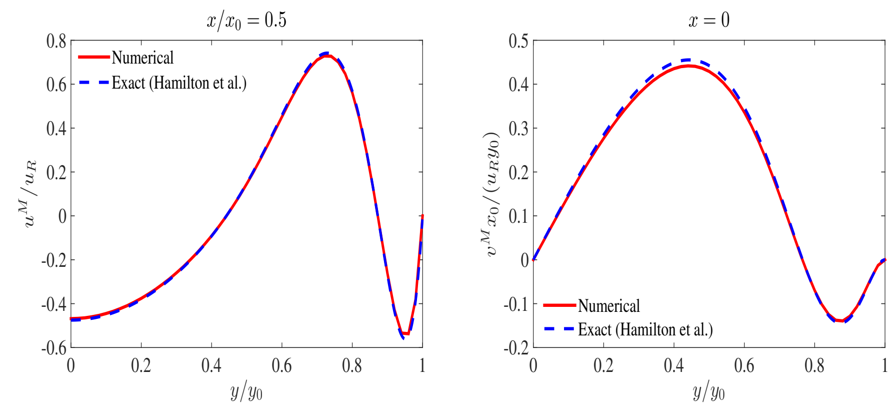

Figure 10: Case 1: Variation of the computed streaming velocity as a function of y/y_0 for the u component at $x = 3L/4$ (left) and for the v component at $x = L/2$ (right)

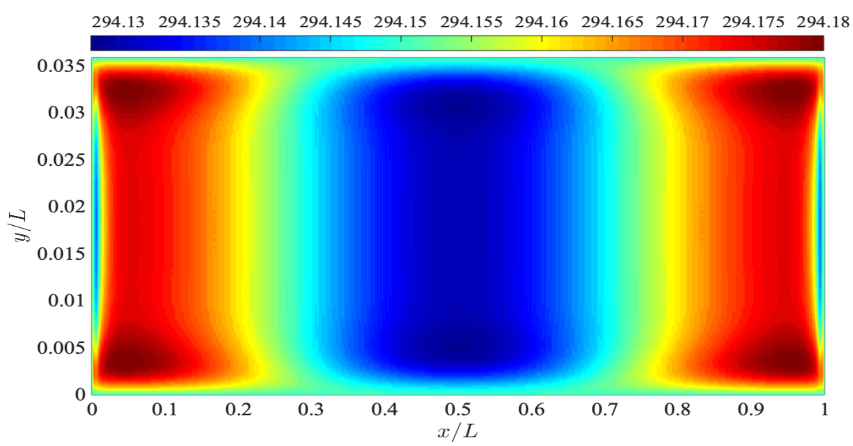

Figure 11: Case 1: mean temperature field along the enclosure

4.3. From slow to fast streaming and filtering

Before proceeding to the next cases where we aim to resolve flows at higher acoustic levels, we have to investigate the use of filtering necessary to obtain converged and stable solutions. This stems from the fact that larger displacements of the enclosure create larger pressure amplitudes while at the same time pressure gradients increase. This leads to sharp (shock-type) profiles which indicate the presence of higher harmonics in the wave field. Similarly wider enclosures i.e. for larger values of the ratio $y_0/\delta\nu$, the viscous effects are weaker and shear forces along the top and bottom walls have less effect on the bulk of the gas leading again to shock-type profiles due to less attenuation.

Aiming to investigate the effect of the parameter a_f, see Section 3.4, two intermediate cases are shown here to exhibit the effect of filtering as the Re_{NL} increases, one with $Re_{NL} = 0.890$ and $Re_{NL} = 2.368$. Figure 12 presents the velocity distributions along the symmetry of the $y-$axis in the enclosure during the 20th period. Referring to the top of Figure 12, it can be observed that as the Re_{NL} increases the solution obtained with the core scheme C3-4-6-4-3, although convergent, contains oscillations with increasing amplitude. These oscillations are located around the shock for the smaller Re_{NL} case, while in higher acoustic levels these are diffused throughout the whole solution. The application of the filtering scheme F(b):B6-B6-I6-B6-B6^{a_f} for two different values, 0.49 and 0.47, of the a_f parameter are shown next. As it can be observed, for the lower Re_{NL} case the oscillations disappear from the solution even for the larger a_f value (where in essence less filtering intensity is applied). On the other hand, for the higher Re_{NL} value case, higher filtering intensity was necessary to reduce the amount of oscillations present in the solution up to an acceptable level.

Following from an extensive study of the different filtering options that can be implemented for the simulations at hand, we have concluded that the choice of the filtering scheme F(b):B6-B6-I6-B6-B6^{a_f} with $a_f \in [0.45, 0.5)$ was sufficient for the test cases that follow, unless otherwise stated.

4.4. Case 2

In this test case the same enclosure width, with $y_0/\delta\nu = 10$, as in Case 1 is considered but the amplitude of the enclosure's displacement is increased to $x_{\max} = 80\mu m$, resulting now in $Re_{NL} = 4.327$. As noted in the Remark previously, for cases with $Re_{NL} > 4$ the filtering option F(d):B6-B6-I6-B6-B6^{a_f} was applied with $a_f = 0.45$ for the filtering intensity. As can be seen in Figure 13, the acoustic velocity signal, in this case, is distorted from the perfect sinusoidal form of the previous cases due to the presence of odd harmonics

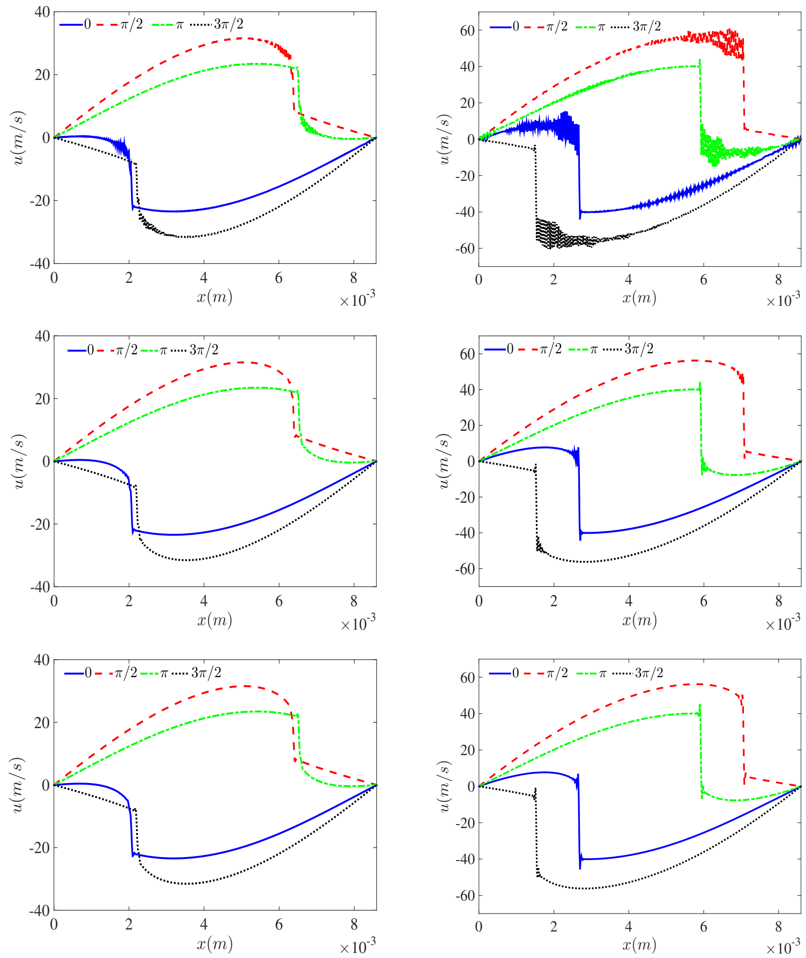

Figure 12: Filtering effect for $Re_{NL} = 0.890$ (left column) and $Re_{NL} = 2.386$ (right column) with no filtering (top), $a_f = 0.49$ (middle) and $a_f = 0.47$ (bottom)

reaching a maximum speed of $71.52 m/s$.

As stated previously, the larger displacement of the enclosure leads to sharp (shock-type) profiles which indicate the presence of higher harmonics in the wave field. This is evident also in Figure 14 which presents the velocity and pressure distributions along the symmetry of the $y-$axis in the enclosure, during the 80th period. Pressure waves emanated from the sinusoidal displacement of the enclosure are strongly distorted by the nonlinear effects. The traveling shock-type waves are of weak intensity and the numerical oscillations produced by the numerical solver remain bounded and thus do not spoil the solution.

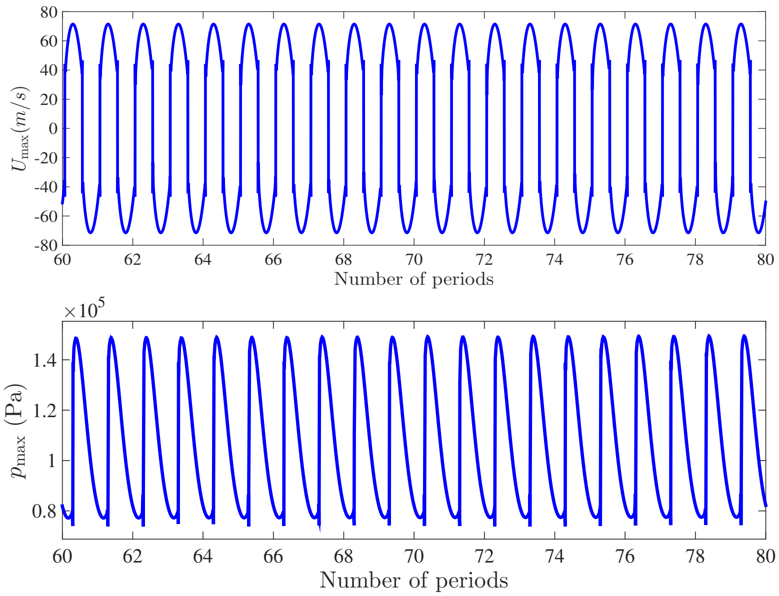

Figure 13: Case 2: Acoustic velocity (top) at the center of the enclosure and pressure (bottom) at the of the enclosure at $x = L$, as functions of the number of periods elapsed

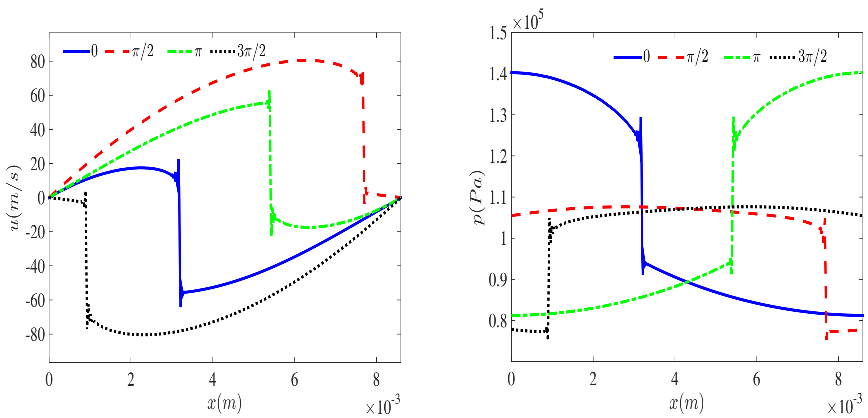

Figure 14: Case 2: Variation of the u velocity (left) and pressure along the symmetry axis at $\omega t = 0, \pi/2, \pi, 3\pi/2$

In this case the re-circulation cells start to become asymmetric as can be seen in Figure 15 where the streamlines of the mean flow field are presented. In this test case, the maximum value for the streaming velocity u^M is found to be approximately $3.421 m/s$.

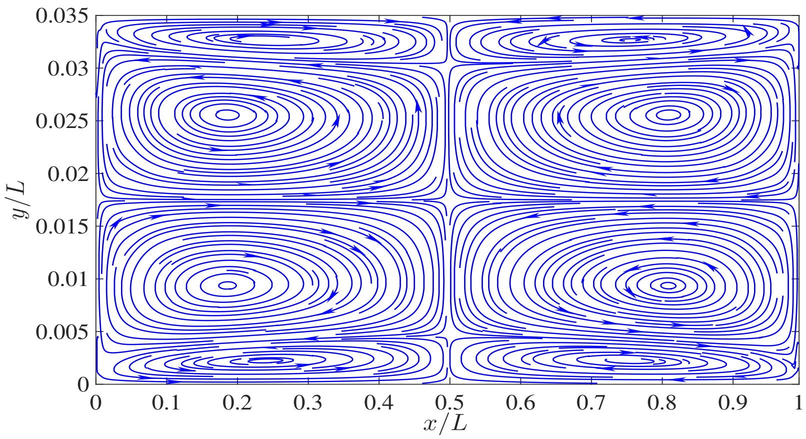

Figure 15: Case 2: streamlines of the numerical mean flow along the enclosure

For this case the mean temperature field starts to become two-dimensional, as shown in Figure 16, due to convective heat transport by the streaming flow as well as heat conduction in both directions. As the Re_{NL} number increases, acoustic streaming becomes an effective means of heat transport resulting in the re-distribution of the mean fluid temperature. Thus, streaming convects the heat along the enclosure's axis from the warmer areas near the vertical walls towards the enclosure's center. The mean temperature difference computed inside the enclosure is now $\Delta T \approx 6.65K$.

4.5. Case 3

In this test case the enclosure width increases giving a ratio of $y_0/\delta\nu = 40$ and the amplitude of the enclosure's displacement is $x_{\max} = 10\mu m$, resulting now in $Re_{NL} = 9.403$. Again, as can be seen in Figure 17, the acoustic velocity signal in this case is again distorted from the perfect sinusoidal form, reaching a maximum primary oscillatory velocity of $26.35 m/s$).

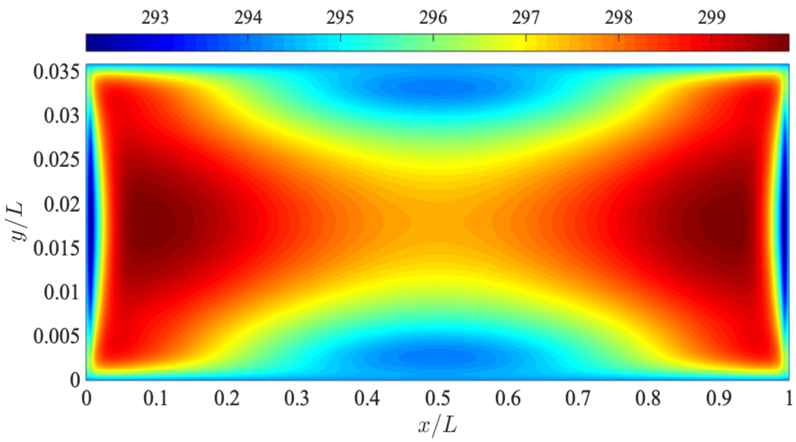

Figure 16: Case 2: mean temperature field along the enclosure

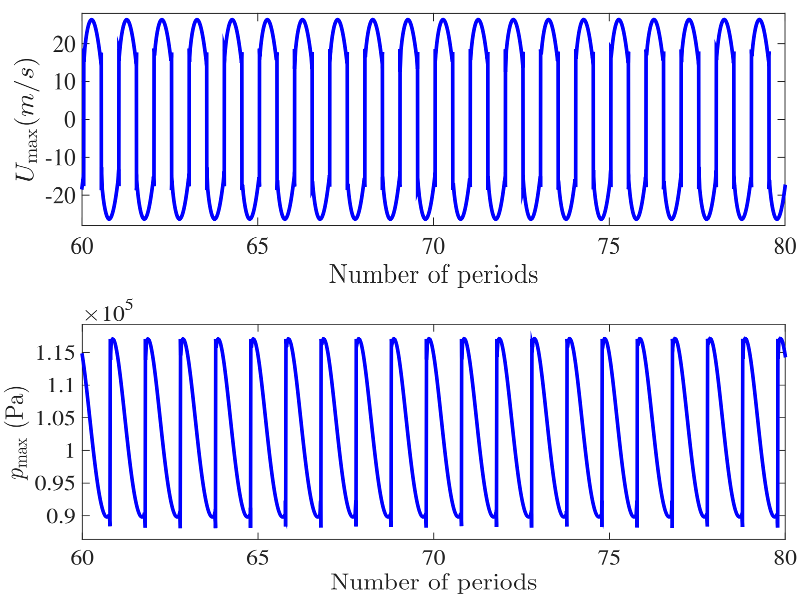

Figure 17: Case 3: Acoustic velocity (top) at the center of the enclosure and pressure (bottom) at the of the enclosure at $x = L$, as functions of the number of periods elapsed

This is evident also in Figure 18 which presents the velocity and pressure distributions along the symmetry of the $y-$axis in the enclosure, during the 80th period. Pressure waves emanating from the displacement of the enclosure are again strongly distorted by the nonlinear effects and since we have a wider enclosure ($y_0/\delta_\nu = 40$) in this case, the viscous effects are weaker and shear forces along the top and bottom walls have a lesser effect on the bulk of the gas leading to higher pressure amplitudes. The shock-wave profiles in velocity and pressure that appear now due to the low attenuation and the numerical oscillations produced by the numerical solver again remain bounded and do not spoil the final solution.

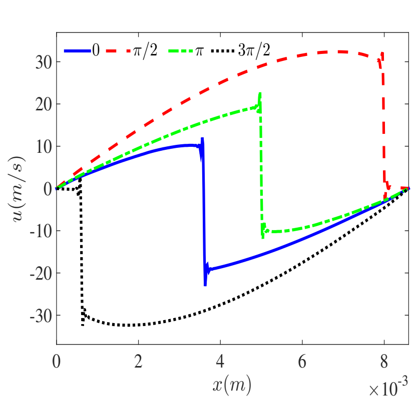

Figure 18: Case 3: Variation of the u velocity (left) and pressure along the symmetry axis at $\omega t = 0, \pi/2, \pi, 3\pi/2$

In this case, the re-circulation cells have become asymmetric and the centers of all streaming cells are displaced towards the lateral walls of the enclosure as can be seen in Figure 19 where the streamlines of the mean flow field are presented. The maximum value for the streaming velocity u^M is found to be approximately $0.830 m/s$. For this case, the mean temperature field, shown in Figure 20, has become two-dimensional due to convective heat transport by the streaming flow as well as heat conduction in both directions. The mean temperature difference inside the enclosure is now $\Delta T \approx 2.67K$ which is smaller compared to the previous case since the Mach number is much smaller compared to the one in Case 2.

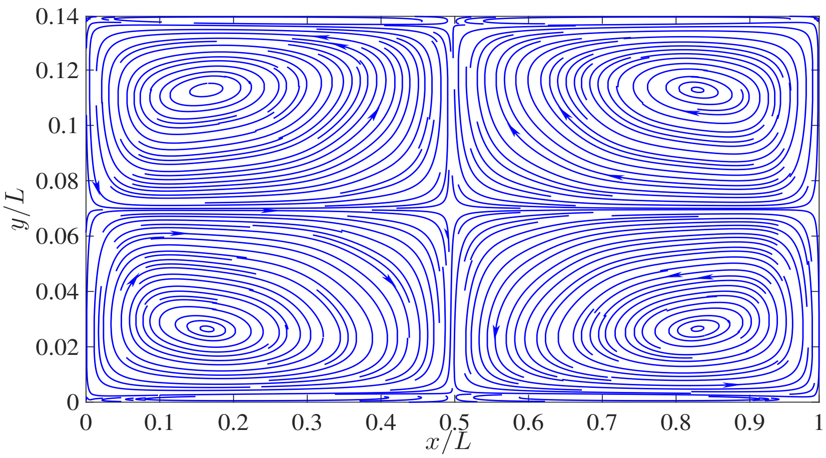

Figure 19: Case 3: streamlines of the numerical mean flow along the enclosure

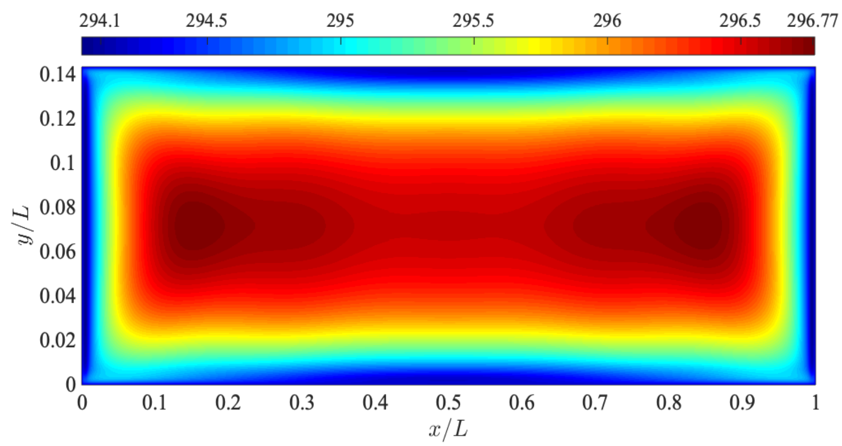

Figure 20: Case 3: mean temperature field along the enclosure

4.6. Case 4

In this test case the enclosure width is half of that in the previous case, giving a ratio of $y_0/\delta\nu = 20$ and the amplitude of the enclosure's displacement is $x_{\max} = 50\mu m$, resulting in a higher $Re_{NL} = 12.723$. In Figure 21 the higher acoustic velocity signal, reaching a maximum value of $61.32m/s$ for this case, can be seen, while Figure 22 presents the velocity and pressure distributions along the symmetry of the $y-$axis in the enclosure during the 100th period.

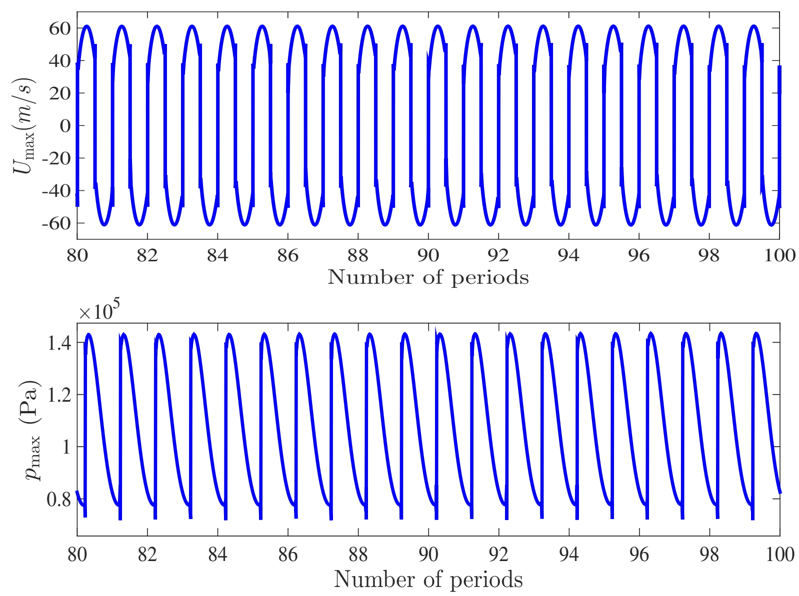

Figure 21: Case 4: Acoustic velocity (top) at the center of the enclosure and pressure (bottom) at the of the enclosure at $x = L$, as functions of the number of periods elapsed

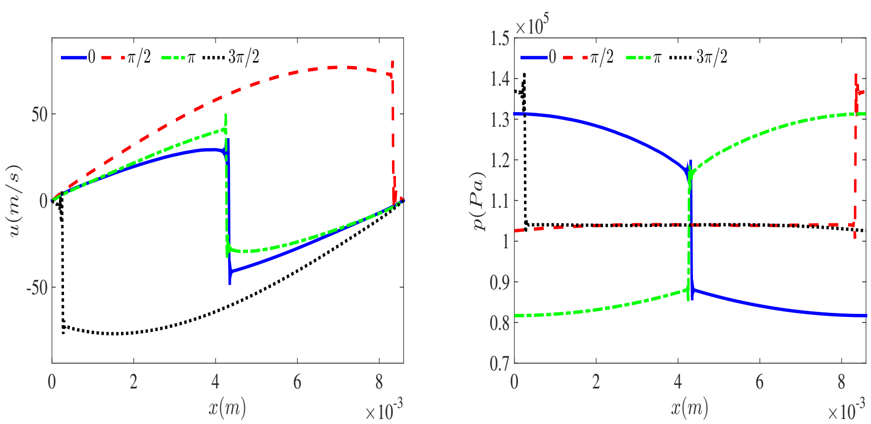

Figure 22: Case 4: Variation of the u velocity (left) and pressure along the symmetry axis at $\omega t = 0, \pi/2, \pi, 3\pi/2$

In Figure 23 the obtained streamlines of the mean flow field are shown. As it was pointed out in [13], there is a change of regime for the temperature

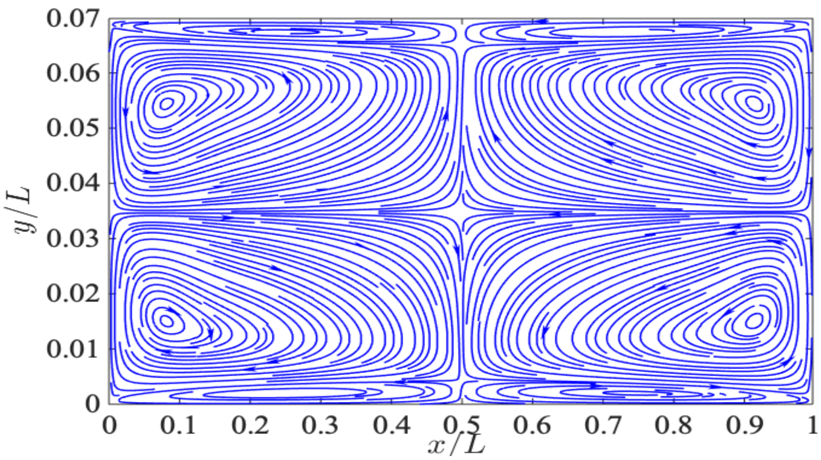

Figure 23: Case 4: streamlines of the numerical mean flow along the enclosure

field before $Re_{NL} = 13.26$, which corresponds to shift of the outer streaming cells towards the velocity node (close to the lateral walls of the enclosure). Hence, a zone of very small streaming velocities is generated in the middle of the cavity which induces the accumulation of heat while the maximum value for the streaming velocity u^M was found to be approximately $2.829 m/s$. This behavior is also evident in the results presented in Figure 24. The mean temperature difference inside the enclosure has now increased to $\Delta T \approx 17.7K$.

4.7. Case 5

In this challenging test case the enclosure has again a ratio of $y_0/\delta\nu = 20$ but the amplitude of the enclosure's displacement is now $x_{\max} = 100\mu m$, resulting in a much higher $Re_{NL} = 27.640$. For this test case, it was found appropriate to increase the spatial discretization to a 601×241 mesh thus increasing the number of points to 6 per boundary layer thickness to obtain a grid independent solution. Further, it was found that the filtering scheme had to be modified using the F(d):B4-B6-I6-B6-B4^{a_f} option i.e. reducing the filtering order at the first layer of grid points close to the boundary, with $a_f = 0.45$.

In Figure 25 the higher acoustic velocity signal for this case can be seen reaching a maximum value of $90.38 m/s$ along with an increase in the pressure

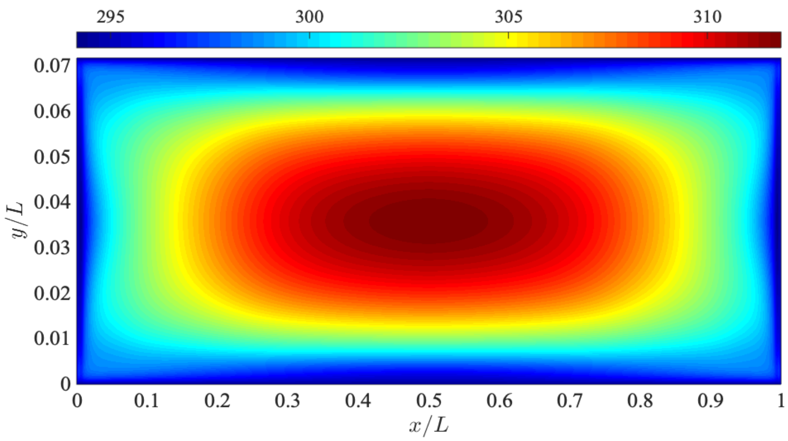

Figure 24: Case 4: mean temperature field along the enclosure

at the lateral boundaries, while Figure 26 presents the velocity and pressure distributions along the symmetry of the $y-$axis in the enclosure, during the 120th period. Compared to Case 4, the larger (doubled) enclosure displacement creates higher pressure amplitudes. As can be seen in the results, although some oscillations are still evident in the numerical solution, these remain bounded and do not spoil the numerical solution.

As can be seen in Figure 27, the outer streaming cells are now split into several cells. The maximum value for the streaming velocity u^M is found to be approximately $4.702m/s$. According to [13], there is an intricate coupling between the mean temperature field and the streaming flow. To this end, the mean temperature gradient in high Re_{NL} numbers changes the orientation and is considered to be the cause of the splitting of the outer streaming cells. It was observed, also in this work, that for this test case, and for a few tens of periods, regular streaming flow appeared. Then, destabilization was observed along with increasing heterogeneity of the mean temperature field, shown in Figure 28. The mean temperature difference inside the enclosure has now increased to $\Delta T \approx 44.66K$ which is almost exactly the value obtained in [13].

Finally, the longitudinal variation along the enclosure's central axis at $y = 0$

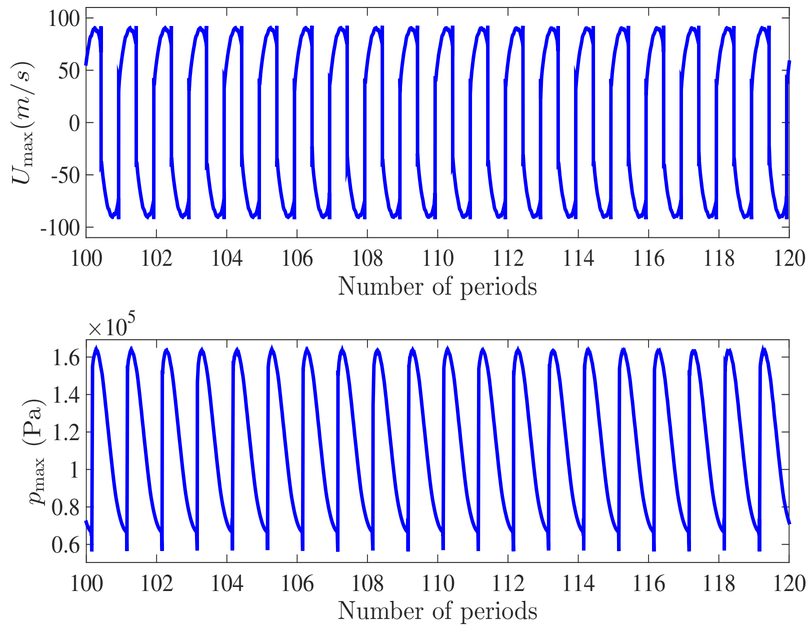

Figure 25: Case 5: Acoustic velocity (top) at the center of the enclosure and pressure (bottom) at the of the enclosure at $x = L$, as functions of the number of periods elapsed

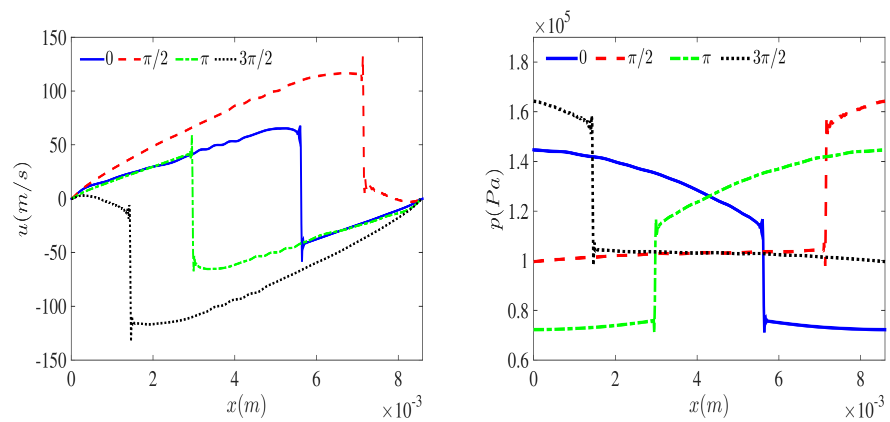

Figure 26: Case 5: Variation of the u velocity (left) and pressure along the symmetry axis at $\omega t = 0, \pi/2, \pi, 3\pi/2$

(an acoustic velocity node) of the axial dimensionless streaming velocity u^M is shown in Figure 29 for test cases 1-5. As it can be seen, the velocity profile

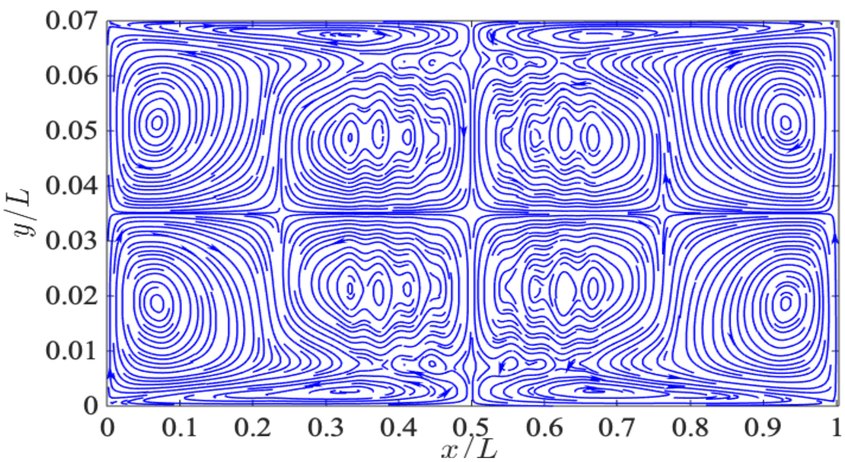

Figure 27: Case 5: streamlines of the numerical mean flow along the enclosure

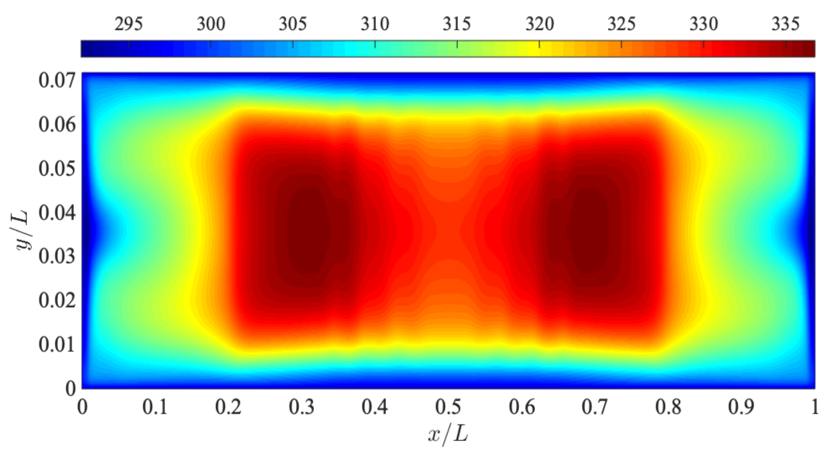

Figure 28: Case 5: mean temperature field along the enclosure

is modified as the Re_{NL} number increases; the sinusoidal form associated with slow (almost linear) streaming becomes steeper near the enclosure's side walls while the average slope of the curves at the center decreases approaching zero at $Re_{NL} = 12.723$. Following from the displacement of the streaming cells, the parabolic behavior of the streaming velocity along the width of the enclosure disappears as the Re_{NL} value increases as shown in Figure 30. These distortions of the streaming cells, as well as the previously presented results, are in agreement with those that have been observed in experiments in rectangular or cylindrical geometries in wide channels, e.g. in [9, 40, 10, 11]. As pointed out in [13], the slope is close to zero for a critical Re_{NL} value between 13 and 27, and then the slope changes sign which indicates the emergence of new streaming cells. This change of the slope sign can also be seen in our results for $Re_{NL} = 27.640$ in Figure 29. Moreover, this is in accordance with the experimental results in [10] where streaming in square enclosures was analyzed and it was found that for Re_{NL} values up to 25, streaming cells are regular whereas when Re_{NL} exceeds 25, streaming deforms to irregular and complex shape patterns.

Moreover, and concerning the mean temperature variation, in [18] a criterion has been established that relates the physical properties of the problem to the transverse temperature difference which flags for a transition in the streaming patterns if

$$\Delta T \geq T_0 \frac{45}{2} \left(1 + \frac{2}{3} \frac{(\gamma - 1)\sqrt{Pr}}{1 + Pr} \right) \left(\frac{\delta_\nu}{y_0} \right)^2 . \tag{41}$$

In our test cases 4 and 5 the corresponding transition value in temperature difference is 18.7230 and only in case 5 ΔT exceeds this threshold verifying further the obtained results.

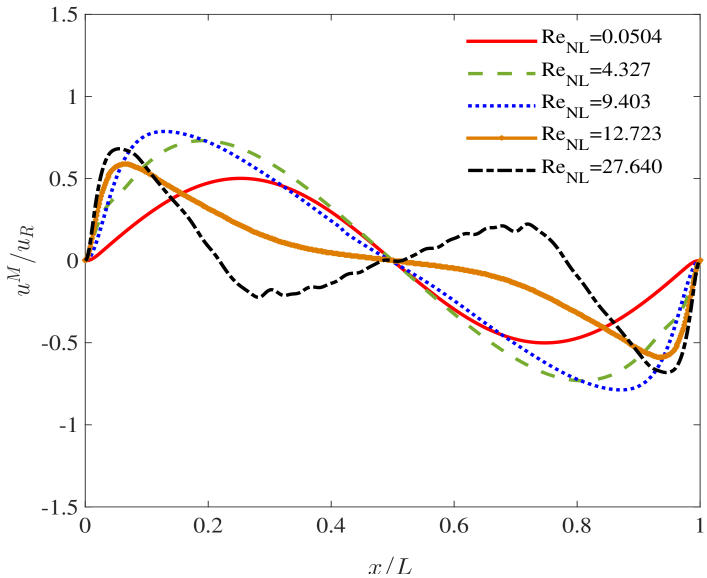

Figure 29: Cases 1-5: comparison of the longitudinal variation of the normalized horizontal streaming velocities u^M

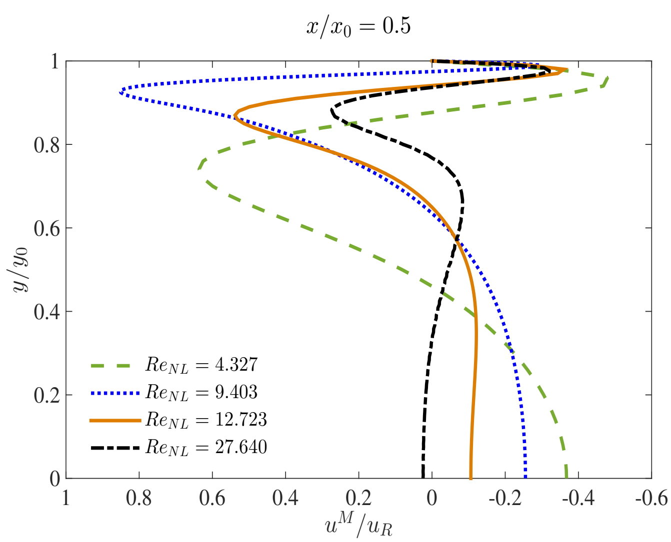

Figure 30: Cases 2-5: comparison of the normalized horizontal streaming velocities u^M along the width of the enclosures

4.8. Case 6

In this final test case, the enclosure has a ratio of $y_0/\delta\nu = 60$, which is three times bigger than that in the last two cases, and the amplitude of the enclosure's displacement is now $x_{\max} = 35\mu m$, resulting in a very big $Re_{NL} \approx 120$. For this test case, the spatial discretization to 301×601 mesh points since the size of the enclosure has increased along the $y-$direction. The same filtering scheme as in test case 5 was adopted here as well. We aim here to study the development of the streaming flow over time.

As can be seen in Figure 31, by $T = 50$ time periods eight different clock-wise and counter clock-wise vortices in the resonator can be seen, while the flow structure is symmetric with respect to both the horizontal and the vertical mid-planes. The resulting temperature field and the generation of a temperature gradient can be seen in Figure 32 (top). At later times, the flow field changes from a quasi-one-dimensional to a two-dimensional leading to an increase in the number of streaming vortices with an irregular streaming structure. At $T = 200$ periods it is important to note that the orientation of the streaming votrices has changed and new smaller vortices have been created, near the velocity nodes, along with an increase in the mean temperature heterogeneity and gradient, while the flow structure remains symmetric with respect to both the horizontal and the vertical mid-planes. At $T = 300$ periods the symmetry of the streaming structure with respect to the vertical mid-plane is distorted (due to the nonlinearity effects) and the generation of secondary vortex rings can be observed. By time $T = 400$ periods more irregular and multiple deformed vortex patterns can be seen while the streaming structure with respect to the vertical mid-plane is further distorted. A mean temperature difference inside the enclosure has been established to $\Delta T \approx 37.85K$. We note here that, the maximum obtained values of the streaming velocity u^M for test Cases 1-6 were: $0.0280, 3.421, 0.830, 2.829, 4.702$ and 3.866, respectively, while the maximum values of the v^M were: $0.000832, 0.200, 0.142, 0.528, 1.187$ and 1.169. We can observe that the ratio $v^M_{max}/u^M_{\max}$ increases from 2.9×10^{-2} to 3×10^{-1} i.e. one order in magnitude. This means that the $y-$component of the streaming velocity has a significant influence on the average flow field and enhances the two-dimensional nature of the problem. The obtained velocity signal at the center of the enclosure and pressure variation at the enclosure's end as functions of the number of the last ten periods is shown in Figure 33. Further, it was found that in this case the streaming patterns were almost stationary and time-invariant after the oscillation had reached a quasi-steady state as can be seen in Figure 34 where the variation of the velocity and pressure along the symmetry axis at $\omega t = 0$ for $T = 200, 300$ and 400 is shown. This is also verified by the comparison of the normalized horizontal streaming velocities u^M along the width of the enclosure for $T = 300$ and $T = 400$ time periods in Figure 35.

Finally, we use this, computationally demanding, test case as to provide an indication of the proposed numerical solver's efficiency. The numerical solver has been implemented, and reasonably optimized, using OpenMP parallel environment using a multi-core processor. The parallel machine used was the Dell R730 server that features two 8-core Xeon E5-2695@2.4GHz processors, with 16GB of memory. The results of the computational times and the obtained speedup are summarized in Table 4 for two grids, a coarser and a finer one along the $x-$direction. the previous numerical results have been obtained with the finer grid and execution times are reported for the computation of $T = 400$ periods.

Table 4: Computational times and speed up for Case 6

	Grid A: 151x601		Grid B: 301x601	
# cores	time (hours)	speedup	time (hours)	speedup
1	129.22	-	282.67	-
2	74.83	1.727	154.61	1.828
4	39.45	3.276	81.33	3.476
8	24.89	5.192	50.78	5.567
16	18.10	7.139	34.43	8.210

From the obtained times, it is evident that very good performance scalability is achieved versus a single-core CPU . As follows from Table 4, speedup factors are increased adding more cores in the computation. Using up to 4 cores the acceleration is almost linear. The best multi-core acceleration factor of the numerical solver is about 8x when all available cores of the machine were enabled and for the finer discretization grid.

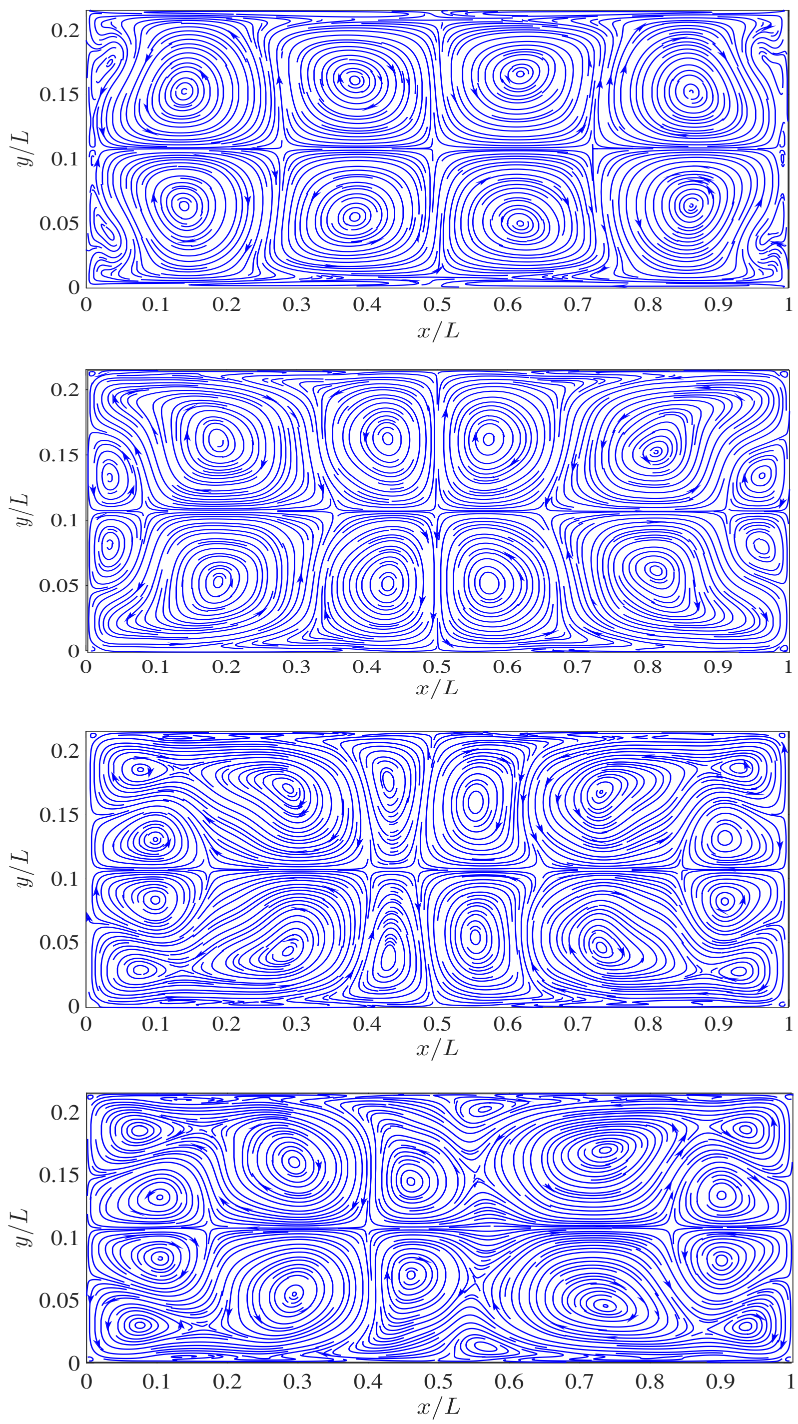

Figure 31: Case 6: streamlines of the numerical mean flow along the enclosure at $T = 50, 200, 300, 400$ periods (from top to bottom)

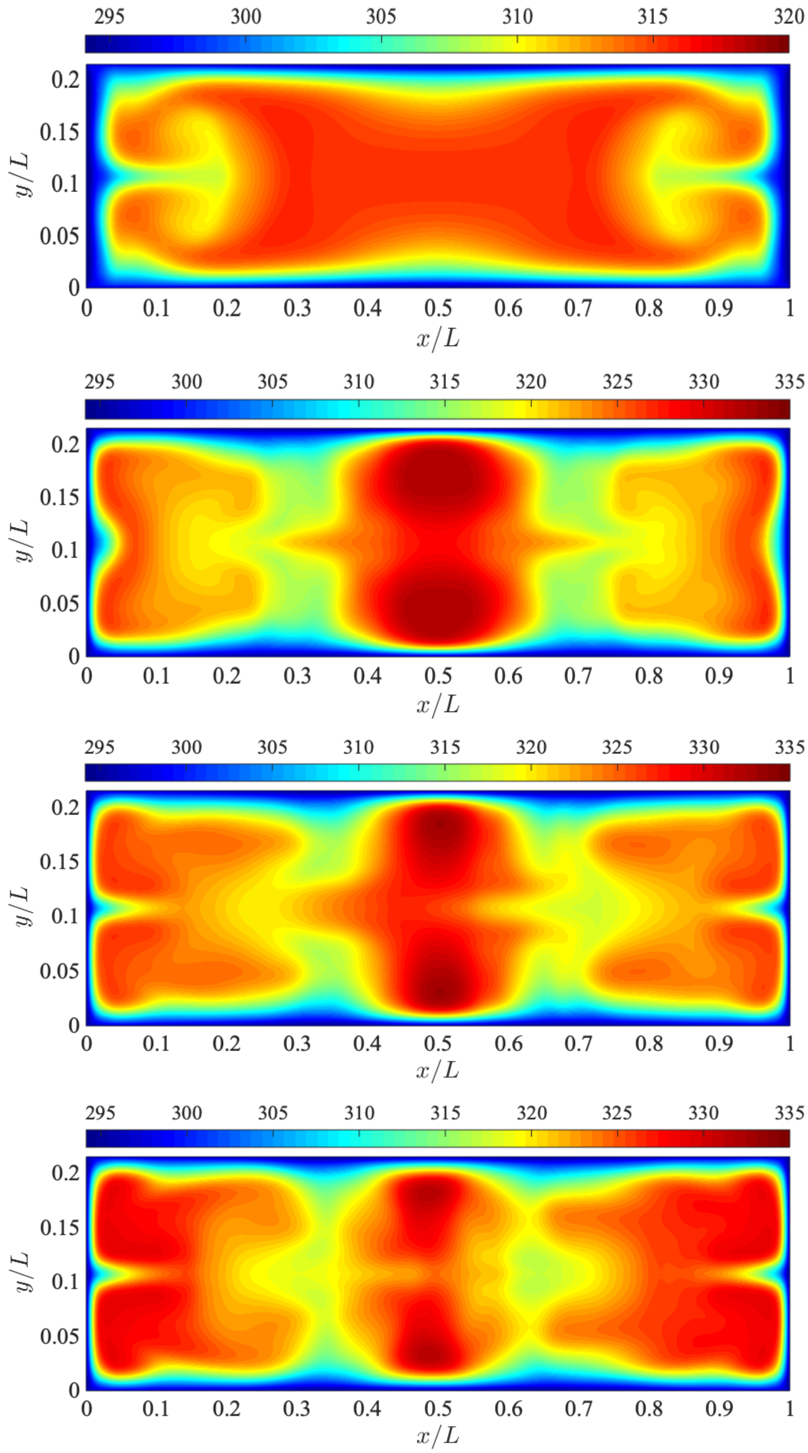

Figure 32: Case 6: mean temperature field along the enclosure at $T = 50, 200, 300, 400$ periods (from top to bottom)

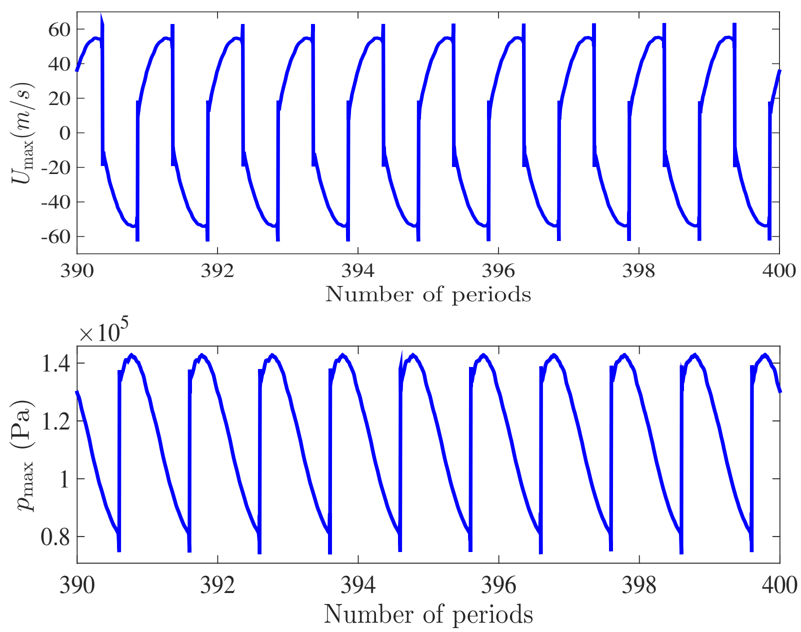

Figure 33: Case 6: Acoustic velocity (top) at the center of the enclosure and pressure (bottom) at the of the enclosure at $x = L$, as functions of the number of periods elapsed

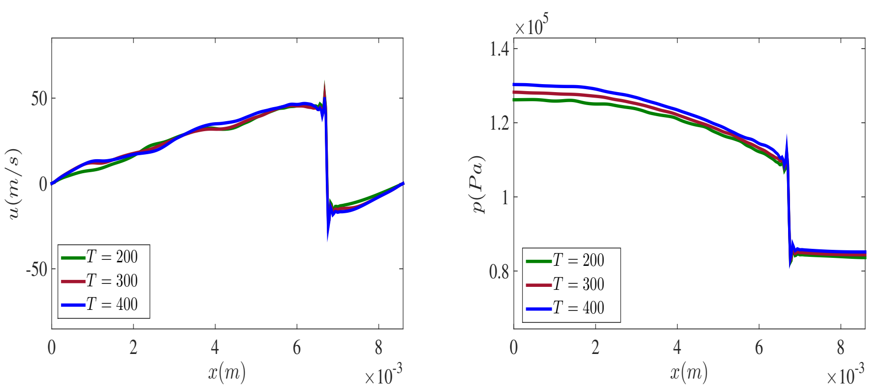

Figure 34: Case 6: Variation of the u velocity (left) and pressure along the symmetry axis at $\omega t = 0$ at $T = 200, 300, 400$

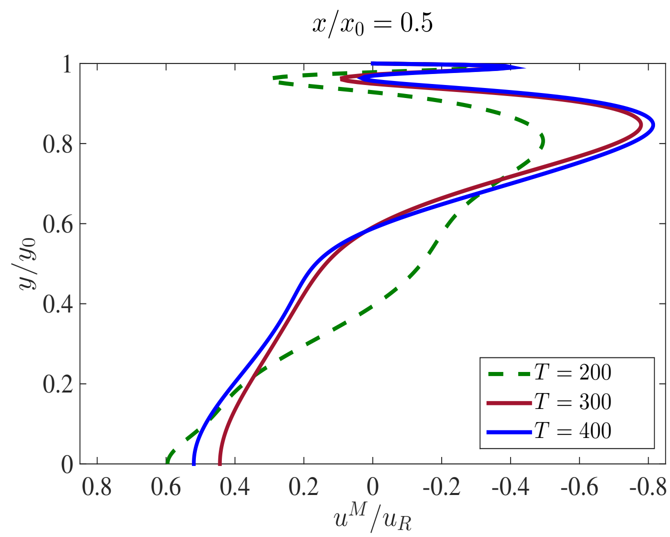

Figure 35: Case 6: comparison of the normalized horizontal streaming velocities u^M along the width of the enclosure for $T = 200, 300, 400$ time periods

5. Conclusions

The formation of acoustic streaming patterns (of the Rayleigh type) and associated flows in rectangular enclosures, with different aspect ratios and amplitudes of displacement, has been studied by solving numerically the unsteady two-dimensional compressible Navier-Stokes equations using a high-order compact finite difference scheme. The acoustic field in the enclosures has been created by a plane standing wave excited inside the enclosures by a harmonic velocity law. Several details of the proposed numerical scheme and its applicability have been given with emphasis on the filtering technique applied to ensure the stability of the solutions in the presence of shock-type waves that may appear in the flow. Several test cases have been considered ranging from linear to highly nonlinear streaming regimes. The numerical simulations performed demonstrated the ability of the proposed numerical scheme to compute the transition from regular acoustic streaming flow toward irregular streaming. While retaining its formal order of accuracy, the numerical scheme produced very accurate results in the linear (and almost linear) cases when compared to known analytical solutions. For the nonlinear cases, the numerical scheme was able to reproduce the significant distortions of the streaming cells where the centers of the streaming cells are pushed towards the end-walls of the enclosures as well as the deformation of the streaming cells that split into several cells for the higher nonlinear cases. The coupling between streaming effects and thermal effects in the enclosures, by the existence and evolution of a mean temperature gradient, has been also investigated. Most of the presented results are in accordance with results presented in the literature from numerical and/or experimental studies.

From this study, it can be concluded that the compact finite difference scheme is capable of simulating the nonlinear acoustic streaming in compressible viscous fluids. Moreover, it can also be concluded that the proposed numerical scheme can be accurate and robust for simulations of highly nonlinearity levels and different enclosure geometries and can be potentially applied to different types of fluids in simulating the nonlinear thermo-acoustic fields. The numerical algorithm can be relatively straightforwardly extended for the case of cylindrical (or curvilinear) coordinates to numerically simulate acoustic streaming in tubes. In this work, the numerical solver has been implemented, and reasonably optimized, using OpenMP parallel environment using a multi-core processor and very good performance scalability was achieved. Furthermore, the entire algorithm can be parallelized efficiently, since in each Runge-Kutta stage several tri-diagonal systems can be solved simultaneously (of order $O(N_x)$). Further, these tri-diagonal systems that arise from the compact discretizations involve only two matrices, one for the computation of the derivatives and one for the filtering, minimizing the required data storage of the algorithm, therefore permitting one to perform the whole computation on an acceleration device, e.g GPUs. To this end, the parallel attributes of the algorithm permit two levels of parallelization which are currently in progress.

Acknowledgment

A.I. Delis wishes to thank INRIA-Nice Sophia Antipolis University team CASTOR for the hospitality while contacting part of the presented research.

References

[1] L. Rayleigh, On the circulation of air observed in Kundts tudes, and some allied acoustical problems, International Journal of Aeroacoustics 2 (3) (2003) 255–292.

[2] M. Lighthill, Acoustic streaming, Journal of Sound and Vibration 61 (3) (1978) 391 – 418.

[3] W. Nyborg, Acoustic streaming, in: M. Hamilton, D. Blackstock (Eds.), Nonlinear Acoustics, Academic Press, San Diego, 1998, pp. 207–231.

[4] S. Boluriaan, P. Morris, Acoustic streaming: From Rayleigh to today, International Journal of Aeroacoustics 2(3) (2003) 255–292.

[5] J. Wu, Acoustic streaming and its applications, Fluids 3 (4) (2018).

[6] L. Menguy, J. Gilbert, Non-linear acoustic streaming accompanying a plane stationary wave in a guide, Acustica 86 (2) (2000) 249–259.

[7] M. Hamilton, Y. Ilinskii, E. Zabolotskaya, Acoustic streaming generated by standing waves in two-dimensional channels of arbitrary width, Journal of the Acoustical Society of America 113 (1) (2003) 153–160.

[8] M. Hamilton, Y. Ilinskii, E. Zabolotskaya, Thermal effects on acoustic streaming in standing waves, Journal of the Acoustical Society of America 114 (6) (2003) 3092–3101.

[9] M. Thompson, A. Atchley, M. Maccarone, Influences of a temperature gradient and fluid inertia on acoustic streaming in a standing wave, Journal of the Acoustical Society of America 117 (4 I) (2005) 1839–1849.

[10] M. Nabavi, K. Siddiqui, J. Dargahi, Analysis of regular and irregular acoustic streaming patterns in a rectangular enclosure, Wave Motion 46 (5) (2009) 312–322.

[11] I. Reyt, V. Daru, H. Bailliet, S. Moreau, J.-C. Valière, D. Baltean-Carlès, C. Weisman, Fast acoustic streaming in standing waves: Generation of an additional outer streaming cell, Journal of the Acoustical Society of America 134 (3) (2013) 1791–1801.

[12] I. Reyt, H. Bailliet, J.-C. Valière, Experimental investigation of acoustic streaming in a cylindrical wave guide up to high streaming reynolds numbers, Journal of the Acoustical Society of America 135 (1) (2014) 27–37.

[13] V. Daru, D. Baltean-Carlès, C. Weisman, P. Debesse, G. Gandikota, Two-dimensional numerical simulations of nonlinear acoustic streaming in standing waves, Wave Motion 50 (5) (2013) 955–963.

[14] V. Daru, I. Reyt, H. Bailliet, C. Weisman, D. Baltean-Carlès, Acoustic and streaming velocity components in a resonant waveguide at high acoustic levels, Journal of the Acoustical Society of America 141 (1) (2017) 563–574.

[15] V. Daru, C. Weisman, D. Baltean-Carlès, I. Reyt, H. Bailliet, Inertial effects on acoustic Rayleigh streaming flow: Transient and established regimes, Wave Motion 74 (2017) 1–17.

[16] M. Červenka, M. Bednařík, Effect of inhomogeneous temperature fields on acoustic streaming structures in resonators, Journal of the Acoustical Society of America 141 (6) (2017) 4418–4426.

[17] M. Červenka, M. Bednařík, Numerical study of the influence of the convective heat transport on acoustic streaming in a standing wave, Journal of the Acoustical Society of America 143 (2) (2018) 727–734.

[18] V. Daru, C. Weisman, D. Baltean-Carlès, H. Bailliet, Acoustically induced thermal effects on Rayleigh streaming, Journal of Fluid Mechanics 911 (2021).

[19] V. Daru, C. Weisman, D. Baltean-Carlès, H. Bailliet, A numerical study of the coupling between Rayleigh streaming and heat transfer at high acoustic level, Journal of the Acoustical Society of America 150 (1) (2021) 4501–4510.

[20] S. Boluriaan, P. Morris, Numerical simulation of acoustic streaming in high amplitude standing waves, in: 9th AIAA/CEAS Aeroacoustics Conference and Exhibit, 2003.

[21] M. Aktas, B. Farouk, Numerical simulation of acoustic streaming generated by finite-amplitude resonant oscillations in an enclosure, Journal of the Acoustical Society of America 116 (5) (2004) 2822–2831.

[22] H. Feng, X. Zhang, Y. Peng, H. Chen, Numerical simulation of nonlinear acoustic streaming in a resonator using gas-kinetic scheme, Journal of Applied Physics 112 (8) (2012).

[23] A. Boufermel, N. Joly, P. Lotton, M. Amari, V. Gusev, Velocity of mass transport to model acoustic streaming: Numerical application to annular resonators, Acta Acustica united with Acustica 97 (2) (2011) 219–227.

[24] M. Červenka, M. Bednařík, Variety of acoustic streaming in 2d resonant channels, Wave Motion 66 (2016) 21–30. doi:10.1016/j.wavemoti.2016.05.001.

[25] P. Merkli, H. Thomann, Thermoacoustic effects in a resonance tube, Journal of Fluid Mechanics 70 (1) (1975) 161–177. doi:10.1017/S0022112075001954.

[26] H. Bailliet, V. Gusev, R. Raspet, R. Hiller, Acoustic streaming in closed thermoacoustic devices, Journal of the Acoustical Society of America 110 (4) (2001) 1808–1821.

[27] S. K. Lele, Compact finite difference schemes with spectral-like resolution, J. Comput. Physics 103 (1992) 16–42.

[28] L. Thomas, Elliptic problems in linear difference equations over a network, Watson Scientific Computing Laboratory Report Columbia University (1949).

[29] Y. Zhang, J. Cohen, J. Owens, Fast tridiagonal solvers on the gpu, ACM SIGPLAN Notices 45 (5) (2010) 127–136.

[30] V. Mandikas, E. Mathioudakis, A parallel multigrid solver for incompressible flows on computing architectures with accelerators, The Journal of Supercomputing 73 (2017) 4931–4956.

[31] R. Visbal, D. D. Gaitonde, High-order-accurate methods for complex unsteady subsonic flows, AIAA Journal 37 (10) (1999) 1231–1239.

[32] L. Caban, A. Tyliszczak, High-order compact difference schemes on wide computational stencils with a spectral-like accuracy, Computers & Mathematics with Applications 108 (2022) 123–140.

[33] P. Yu, Z. F. Tian, A compact streamfunction–velocity scheme on nonuniform grids for the 2d steady incompressible navier–stokes equations, Computers & Mathematics with Applications 66 (7) (2013) 1192–1212.

[34] E. N. Mathioudakis, V. G. Mandikas, G. V. Kozyrakis, N. A. Kampanis, J. A. Ekaterinaris, Multigrid cell-centered techniques for high-order incompressible flow numerical solutions, Aerospace Science and Technology 64 (2017) 85–101.

[35] D. Fishelov, A new fourth-order compact scheme for the navier–stokes equations in irregular domains, Computers & Mathematics with Applications 74 (1) (2017) 6–25.

[36] J. A. Ekaterinaris, Implicit, high-resolution, compact schemes for gas dynamics and aeroacoustics, Journal of Computational Physics 156 (2) (1999) 272–299.

[37] D. Gaitonde, M. Visbal, High order schemes for Navier-Stokes equations: Algorithm and implementation into FDL3DI, in: NASA, AFRL-VA-WP-TR-1998-3060, 1998.

[38] T. Poinsot, S. Lele, Boundary conditions for direct simulations of compressible viscous flows, Journal of Computational Physics 101 (1) (2092) 104–129.

[39] M. Visbal, D. V. Gaitonde, On the use of higher-order finite-difference schemes on curvilinear and deforming meshes, Journal of Computational Physics 181 (1) (2002) 155 – 185.

[40] S. Moreau, H. Bailliet, J.-C. Valière, Measurements of inner and outer streaming vortices in a standing waveguide using laser doppler velocimetry, Journal of the Acoustical Society of America 123 (2) (2008) 640–647.

Appendix

For completeness, we present here the coefficient values for the different options in the filtering process as described in Section 3.3.

Table 5: Interior Points Coefficients for Different Order Filter Formulas

Schemes (OA)	a_0	a_1	a_2	a_3	a_4
I2 ($K = 1$)	$\frac{1}{2} + \alpha_f$	$\frac{1}{2} + \alpha_f$	0	0	0
I4 ($K = 2$)	$\frac{5}{8} + \frac{3\alpha_f}{4}$	$\frac{1}{2} + \alpha_f$	$\frac{-1}{8} + \frac{\alpha_f}{4}$	0	0
I6 ($K = 3$)	$\frac{11}{16} + \frac{5\alpha_f}{8}$	$\frac{15}{32} + \frac{17\alpha_f}{16}$	$\frac{-3}{16} + \frac{3\alpha_f}{8}$	$\frac{1}{32} - \frac{\alpha_f}{16}$	0
I8 ($K = 4$)	$\frac{93 + 70\alpha_f}{128}$	$\frac{7 + 18\alpha_f}{16}$	$\frac{-7 + 14\alpha_f}{32}$	$\frac{1}{16} - \frac{\alpha_f}{8}$	$\frac{-1}{128} + \frac{\alpha_f}{64}$

Table 6: Coefficients for Boundary Filter Formulas at nodes $2, j$ of 4th and 6th order accuracy

OA	$a_{1,2}$	$a_{2,2}$	$a_{3,2}$	$a_{4,2}$	$a_{5,2}$	$a_{6,2}$	$a_{7,2}$
B4	$\frac{1}{16}+\frac{7\alpha_f}{8}$	$\frac{3}{4}+\frac{\alpha_f}{2}$	$\frac{3}{8}+\frac{\alpha_f}{4}$	$-\frac{1}{4}+\frac{\alpha_f}{2}$	$\frac{1}{16}+\frac{-\alpha_f}{8}$	0	0
B6	$\frac{1}{64}+\frac{31\alpha_f}{32}$	$\frac{15}{64}+\frac{3\alpha_f}{16}$	$\frac{15}{64}+\frac{17\alpha_f}{32}$	$-\frac{5}{16}+\frac{5\alpha_f}{8}$	$\frac{15}{64}-\frac{15\alpha_f}{32}$	$-\frac{3}{32}+\frac{3\alpha_f}{16}$	$\frac{1}{64}-\frac{\alpha_f}{32}$

Table 7: Coefficients for Boundary Filter Formulas at nodes $3, j$ of 6th order accuracy

OA	$a_{1,2}$	$a_{2,2}$	$a_{3,2}$	$a_{4,2}$	$a_{5,2}$	$a_{6,2}$	$a_{7,2}$
B6	$-\frac{1}{64}+\frac{\alpha_f}{32}$	$\frac{3}{32}+\frac{13\alpha_f}{16}$	$\frac{49}{64}+\frac{15\alpha_f}{32}$	$\frac{5}{16}+\frac{3\alpha_f}{8}$	$-\frac{15}{64}+\frac{15\alpha_f}{32}$	$\frac{3}{32}-\frac{3\alpha_f}{16}$	$-\frac{1}{64}+\frac{\alpha_f}{32}$